Localized artificial diffusivity scheme for discontinuity capturing on curvilinear meshes

S. Kawai [a,*], S.K. Lele [b,c]

[a] Center for Turbulence Research, Stanford University, 488 Escondido Mall, Stanford, CA 94305-3035, USA
[b] Department of Aeronautics and Astronautics, Stanford University, 496 Lomita Mall, Stanford, CA 94305-4035, USA
[c] Department of Mechanical Engineering, Stanford University, 496 Lomita Mall, Stanford, CA 94305-4035, USA

ARTICLE INFO

ABSTRACT

A simple and efficient localized artificial diffusivity scheme is developed for the purpose of capturing discontinuities on curvilinear and anisotropic meshes using a high-order compact differencing scheme. The artificial diffusivity is dynamically localized in space to capture different types of discontinuities such as a shock wave, contact surface or material discontinuity. The method is intended for use with large-eddy simulation of compressible transitional and turbulent flows. The method captures the discontinuities on curvilinear and anisotropic meshes with minimum impact on the smooth flow regions. The amplitude of wiggles near a discontinuity and the number of grid points used to capture the discontinuity do not depend on the mesh size. The comparisons between the proposed method and high-order shock-capturing schemes illustrate the advantage of the method for the simulation of flows involving shocks, turbulence and their interactions. The multi-dimensional formulation is tested on a variety of 1D and 2D, steady and unsteady, different types of discontinuity-related problems on curvilinear and anisotropic meshes. A simplification of the method which reduces the computational cost does not show any major detrimental effect on the discontinuity capturing under the conditions examined.

1. Introduction

Due to advances in computational power and numerical algorithms, the application of large-eddy simulation (LES) to transitional and turbulent compressible flows is the focus of significant recent research. The engineering motivation for compressible LES is to provide a more realistic turbulent flowfields than Reynolds-averaged Navier–Stokes simulations and to educidate the unsteady phenomena such as mixing, combustion, heat-transfer, sound-generation and unsteady loads which may be of interest.

Because of their spectral-like resolution, high-order compact differencing schemes [1] are an attractive choice for LES of transitional and turbulent flows to reduce dispersion, anisotropy and dissipation errors associated with the spatial discretization. High-order compact differencing schemes have been applied to practical applications [2–4], and they all have shown the capability of the algorithm. However, these central differencing schemes cannot be applied directly to flows that contain discontinuities. When flows contain steep gradients, such as shock waves, contact surfaces or material discontinuity, non-physical spurious oscillations that make the simulation unstable are generated. The development of numerical algorithms

* Corresponding author. Tel.: +1 650 723 9286.
  E-mail address: skawai@stanford.edu (S. Kawai).

that capture discontinuities and also resolve the scales of turbulence in compressible turbulent flows remains a significant challenge.

Several techniques to extend compact schemes to discontinuous flows have been proposed. Lee et al. [5] proposed a hybrid approach to capture discontinuities. In regions of strong shock waves, the compact differencing of convective fluxes is replaced locally by the essentially non-oscillatory (ENO) scheme [6]. Similarly, Rizzetta et al. [7] introduce hybridization of the compact differencing scheme with Roe's upwind-biased scheme [8]. Visbal and Gaitonde [9] developed an adaptive filter method in which the compact scheme is coupled with a locally reduced-order filter to capture discontinuities. Both approaches require a detector to identify the smooth and non-smooth regions in the flow. The choice of an effective discontinuity detector remains a bottleneck for these methods when applied to complex applications. Additionally, hybrid schemes, such as a hybrid of an accurate linear scheme and a robust non-linear shock-capturing scheme, can possibly cause numerical instabilities when multiple discontinuities are closely located (the grid points separating them are very few).

An attractive alternative to these methods has been proposed by Cook and Cabot [10,11], Fiorina and Lele [12] and Cook [13] by dynamically adding localized high-wavenumber biased artificial diffusivity where needed, to capture discontinuities using high-order compact differencing schemes. The main feature of the artificial diffusivity is to suppress the unresolved high frequency content of the flowfield on a given mesh to capture the discontinuity with minimal effects by smearing the discontinuity over a numerically resolvable scale. Also, in the limit of grid spacing $\Delta \to 0$, the artificial diffusivity vanishes and the governing equations converge to the original Navier–Stokes equations. Main advantages of the method are its simplicity, low computational cost, automatic deactivation in smooth regions (high-resolution characteristics of a high-order compact scheme is preserved in smooth regions), easy to implement in an existing code, design to provide high-wavenumber biased damping, and the lack of a discontinuity detector or weighting/hybrid scheme. All these advantages are desirable for compressible LES of the flows involving shock, contact, and material discontinuities, turbulence and their interactions. In the previous work the method was shown to work well on 1D and 2D shock-related problems. However, most of the test cases in the previous works used uniformly spaced Cartesian coordinate systems. Therefore, the extension of the method to curvilinear and anisotropic meshes is still an open issue. This extension is necessary for the method to be useful for practical applications.

The objective of this paper is to establish the methodology for capturing discontinuities in a curvilinear coordinate framework using a high-order compact scheme. Simple and efficient localized high-wavenumber biased artificial diffusivity scheme on curvilinear and anisotropic meshes is proposed. The original formulation is also simplified to reduce the computational costs while achieving better representation of high-order derivatives. The performance of the method will be assessed on a 2D smooth/non-smooth flows and several 1D and 2D, steady and unsteady, different types of discontinuity-related problems.

2. Mathematical models

2.1. Governing equations

The compressible Navier–Stokes equations for an ideal non-reactive gas are:

$$\frac{\partial \rho}{\partial t} + \nabla \cdot (\rho \boldsymbol{u}) = 0, \tag{1}$$

$$\frac{\partial \rho \boldsymbol{u}}{\partial t} + \nabla \cdot (\rho \boldsymbol{u}\boldsymbol{u} + p\underline{\boldsymbol{\delta}} - \underline{\boldsymbol{\tau}}) = 0, \tag{2}$$

$$\frac{\partial E}{\partial t} + \nabla \cdot [E\boldsymbol{u} + (p\underline{\boldsymbol{\delta}} - \underline{\boldsymbol{\tau}}) \cdot \boldsymbol{u} - \kappa \nabla T] = 0, \tag{3}$$

$$\frac{\partial \rho Y_k}{\partial t} + \nabla \cdot (\rho \boldsymbol{u} Y_k) - \nabla \cdot (\rho D_k \nabla Y_k) = 0, \tag{4}$$

$$E = \frac{p}{\gamma - 1} + \frac{1}{2}\rho \boldsymbol{u} \cdot \boldsymbol{u}, \quad p = \rho R T, \tag{5}$$

where ρ is the density, $\boldsymbol{u}$ is the velocity vector, p is the static pressure, E is the total energy, T is the temperature, γ (=1.4:air) is the ratio of specific heats, R is the gas constant, κ is the thermal conductivity, $\underline{\boldsymbol{\delta}}$ is the unit tensor. Eq. (4) is the transport equation for a mass fraction Y_k where D_k is the species diffusion coefficient. The viscous stress tensor $\underline{\boldsymbol{\tau}}$ is

$$\underline{\boldsymbol{\tau}} = \mu(2\underline{\boldsymbol{S}}) + \left(\beta - \frac{2}{3}\mu\right)(\nabla \cdot \boldsymbol{u})\underline{\boldsymbol{\delta}}, \tag{6}$$

where μ is the dynamic (shear) viscosity, β is the bulk viscosity, and $\underline{\boldsymbol{S}}$ is the strain rate tensor, $\underline{\boldsymbol{S}} = \frac{1}{2}(\nabla \boldsymbol{u} + (\nabla \boldsymbol{u})^{\mathrm{T}})$.

2.2. Localized artificial diffusivity

When a high-order compact scheme is applied to solve flows that involve steep gradients such as those due to shock waves, contact surfaces or material discontinuity, non-physical spurious oscillations that make the simulation unstable

are generated. A key issue here is how to properly remove the non-physical spurious oscillations without damping the resolved scales of turbulence.

Cook [13] introduced a high-wavenumber biased artificial diffusivity to suppress the unresolved high frequency content of the flowfield to capture the discontinuity by smearing the discontinuity over a numerically resolvable scale. The method is based on adding grid-dependent artificial fluid transport coefficients to the coefficients appearing in Eqs. (3), (4) and (6),

$$\mu = \mu_f + \mu^*,$$ (7)

$$\beta = \beta_f + \beta^*,$$ (8)

$$\kappa = \kappa_f + \kappa^*,$$ (9)

$$D_k = D_{f,k} + D_k^*,$$ (10)

where the f subscripts and asterisks denote fluid and artificial transport coefficients. The artificial fluid transport coefficients are designed to vanish in smooth well-resolved regions and provide damping in non-smooth unresolved regions to capture different types of discontinuity. The artificial diffusivity is modeled by [13]

$$\mu^* = C_\mu \overline{\rho |\nabla^r S|} \Delta^{r+2},$$ (11)

$$\beta^* = C_\beta \overline{\rho |\nabla^r S|} \Delta^{r+2},$$ (12)

$$\kappa^* = C_\kappa \overline{\frac{\rho c_s}{T} |\nabla^r e|} \Delta^{r+1},$$ (13)

$$D_k^* = C_D \overline{|\nabla^r Y_k|} \frac{\Delta^{r+2}}{\Delta t} + C_Y \overline{[Y_k - 1]H(Y_k - 1) - Y_k[1 - H(Y_k)]} \frac{\Delta^2}{\Delta t},$$ (14)

where C_μ, C_β, C_κ, C_D and C_Y are user-specified constants, Δ is local grid spacing, S is the magnitude of the strain rate tensor, c_s is sound speed, e is internal energy defined by $e = \frac{1}{\gamma - 1} \frac{p}{\rho}$, and H is the Heaviside function. If r is sufficiently high, the high-wavenumber biased (k^r) artificial diffusivity only damps wavenumbers close to the unresolved wavenumbers. The overbar denotes an approximate truncated-Gaussian filter [10].

Typically, in the method, Δ is defined as the geometrically averaged local grid spacing (cube-root of cell volume), and a value of $r = 4$ is chosen and $\nabla^4 f$ is decomposed to a series of Laplacians, $\nabla^4 f = \nabla^2(\nabla^2 f)$. The typical values for the user-specified constants with $r = 4$ are $C_\mu = 0.002$, $C_\beta = 1$, $C_\kappa = 0.01$, $C_D = 0.003$ and $C_Y = 100$ [13].

Fiorina and Lele [12] introduced the density diffusivity to capture a contact discontinuity instead of using κ^* by adding an additional artificial diffusive term in the continuity of mass equation. However, it is more natural to add κ^* to capture a temperature discontinuity than adding an additional diffusion term to the continuity equation. Also, from a physical viewpoint, density does not diffuse. Therefore, the discontinuity capturing scheme for curvilinear and anisotropic meshes proposed in this paper is essentially based on the original 1D formulation proposed by Cook [13].

2.3. Reformulation for curvilinear and anisotropic meshes

The original properties of the 1D formulation of artificial diffusivity of Cook [13] that capture discontinuities with minimal effects on vorticity should be preserved when the method is reformulated for multi-dimensional curvilinear and anisotropic meshes.

In order to extend the original method to a multi-dimensional curvilinear coordinate system, the Δ scaling appearing in Eqs. (11)–(14) has to be generalized. The use of geometrically averaged grid spacing as proposed in the original paper [13] is one choice that worked well on an isotropic grid. However, the geometrically averaged grid spacing introduces an undesirable mesh dependence when an anisotropic mesh is used. As a simple example, consider the problem of capturing a steady shock wave in 1D flow on a grid spacing defined by $\Delta = \Delta x$, for which the 1D formulation of artificial shear viscosity will be

$$\mu_{1D}^* = C_\mu \overline{\rho \left| \frac{\partial^r S}{\partial x^r} \right|} \Delta x^{r+2}.$$ (15)

When the same 1D shock is considered on a 2D domain, the artificial shear viscosity using the geometrically averaged grid spacing will be

$$\mu_{2D}^* = C_\mu \overline{\rho |\nabla^r S|} (\Delta x \Delta y)^{\frac{r+2}{2}} = \mu_{1D}^* \times \left(\frac{\Delta y}{\Delta x} \right)^{\frac{r+2}{2}}.$$ (16)

If an isotropic grid is used ($\Delta x = \Delta y$), $\mu_{1D}^* = \mu_{2D}^*$ and the artificial diffusion terms behave consistently with the original 1D formulation. However, when an anisotropic grid ($\Delta x \neq \Delta y$) is used, $\mu_{1D}^* \neq \mu_{2D}^*$ and more or less than the necessary diffusion will be introduced. This might cause significant numerical damping of resolved scales of turbulence due to the excessive dissipation or spurious non-physical oscillations across the steep gradients.

To construct a consistent multi-dimensional artificial diffusivity, each term in $|\nabla^r S| \Delta^{r+2}$ needs to be grid-dependent for all possible discontinuity directions. That is, each derivative in $\nabla^r S$ should be scaled by the grid spacing in the derivative direction to avoid the undesirable effects from the grid spacing in other directions. The Gaussian filter removes the cusps intro-

duced by the high-order derivative operators used to compute the artificial diffusivity. Therefore, the grid spacing dependence should be located in the operand of the Gaussian filter. As discussed, in the original methods, the $\nabla^r f$ appearing in Eqs. (11)–(14) is computed by a series of Laplacians and evaluated using a high-order compact differencing scheme. The evaluation of the series of Laplacians induces significant computational cost. Furthermore, considering a multi-dimensional generalized coordinate extension of a series of Laplacians, the full implementation of the Laplacians induces further computational cost in evaluating the additional cross-derivative terms. To reduce the computational costs and achieve better representation of the high derivatives for practical use, an alternative simplification is the direct evaluation of $\sum_{j=1}^{3} \frac{\partial^r f}{\partial x_j^r}$ instead of a series of Laplacians. Hence we evaluate the localized artificial diffusivity on a multi-dimensional generalized coordinate system defined by

$$\mu^* = C_\mu \rho \left| \sum_{l=1}^{3} \left[\sum_{m=1}^{3} \left(\frac{\partial \xi_l}{\partial x_m} \right)^2 \right]^{r/2} \frac{\partial^r S}{\partial \xi_l^r} \Delta_l^{r+2} \right|, \tag{17}$$

$$\beta^* = C_\beta \rho \left| \sum_{l=1}^{3} \left[\sum_{m=1}^{3} \left(\frac{\partial \xi_l}{\partial x_m} \right)^2 \right]^{r/2} \frac{\partial^r S}{\partial \xi_l^r} \Delta_l^{r+2} \right|, \tag{18}$$

$$\kappa^* = C_\kappa \frac{\rho c_s}{T} \left| \sum_{l=1}^{3} \left[\sum_{m=1}^{3} \left(\frac{\partial \xi_l}{\partial x_m} \right)^2 \right]^{r/2} \frac{\partial^r e}{\partial \xi_l^r} \Delta_l^{r+1} \right|, \tag{19}$$

$$D_k^* = C_D c_s \left| \sum_{l=1}^{3} \left[\sum_{m=1}^{3} \left(\frac{\partial \xi_l}{\partial x_m} \right)^2 \right]^{r/2} \frac{\partial^r Y_k}{\partial \xi_l^r} \Delta_l^{r+1} \right| + C_Y c_s \overline{[Y_k - 1]H(Y_k - 1) - Y_k[1 - H(Y_k)]\Delta_{Y_k}}, \tag{20}$$

where ξ_l refers to generalized coordinates ξ, η and ζ and x_m refers to x, y and z when l and m are 1, 2 and 3, respectively. Δ_l is the grid spacing in the physical space along the grid line in the ξ_l direction and is defined by $\Delta_l^2 = \sum_{n=1}^{3} \left(\frac{x_{n,i+1} - x_{n,i-1}}{2} \right)^2$, where $x_{n,i}$ refers to x_i, y_i and z_i when n is 1, 2 and 3 and i is a node index in the ξ_l direction. Δ_{Y_k} in Eq. (20) is the grid spacing in the physical space defined by

$$\Delta_{Y_k} = \frac{\sum_{l=1}^{3} \left| \frac{\partial^r Y_k}{\partial \xi_l^r} \right| \Delta_l}{\sqrt{\sum_{l=1}^{3} \left(\frac{\partial^r Y_k}{\partial \xi_l^r} \right)^2} + \varepsilon}, \tag{21}$$

where ε is the small constant (e.g. $\varepsilon = 10^{-16}$) to prevent division by zero. Note that the proposed D_k^* model is different from the original model of Cook [13] as shown in Eq. (14). The original model for D_k^* has a dependence on the time-step size and introduces higher artificial diffusivity when the time-step size is reduced. Thus, for solution at a fixed physical time, different thickness of material interface are obtained for different time-steps with a same grid and flow. Also, note that due to computational cost, all cross-derivative terms are neglected in Eqs. (17)–(20). This formulation does not make the artificial diffusivity perfectly consistent with the original 1D formulation when multi-dimensional flows are considered because the same value of the artificial diffusion coefficient is applied in every direction. This could potentially have a significant detrimental effect. However, the performance of the overall scheme examined here with test cases for 2D discontinuity-related problems on Cartesian and curvilinear meshes show that this assumption does not have any significant detrimental effect. In the limit of $\Delta_l \to 0$, Eqs. (17)–(20) $\to 0$. Therefore, the governing equations converge to the original Navier–Stokes equations.

In the present study, $r = 4$ is adopted in Eqs. (17)–(20). The fourth derivatives, $\frac{\partial^4 S}{\partial \xi_l^4}$, $\frac{\partial^4 e}{\partial \xi_l^4}$ and $\frac{\partial^4 Y_k}{\partial \xi_l^4}$ are evaluated by [1]

$$\alpha \frac{\partial^4 f_{i-1}}{\partial \xi_l^4} + \frac{\partial^4 f_i}{\partial \xi_l^4} + \alpha \frac{\partial^4 f_{i+1}}{\partial \xi_l^4} = b \frac{f_{i+3} - 9f_{i+1} + 16f_i - 9f_{i-1} + f_{i-3}}{6\Delta \xi_l^4} + a \frac{f_{i+2} - 4f_{i+1} + 6f_i - 4f_{i-1} + f_{i-2}}{\Delta \xi_l^4}. \tag{22}$$

Sixth- and fourth-order tridiagonal schemes and a fourth-order explicit scheme at interior points are obtained by setting the parameters as: sixth-order tridiagonal, $\alpha = \frac{7}{26}$, $a = \frac{19}{13}$ and $b = \frac{1}{13}$ (C6); fourth-order tridiagonal, $\alpha = \frac{1}{4}$, $a = \frac{3}{2}$ and $b = 0$ (C4); fourth-order explicit, $\alpha = 0$, $a = 2$ and $b = -1$ (E4). $\Delta \xi_l$ is the spatial grid size. These schemes are used in the present assessments.

At a near boundary point i, one-sided explicit formulas are utilized:

$$f_i^{''''} = \frac{1}{h^4} \sum_{n=1}^{8} a_{n,i} f_n, \quad i \in 1, 2 \tag{23}$$

$$f_i^{''''} = \frac{1}{h^4} \sum_{n=0}^{7} a_{\mathrm{imax}-n,i} f_{\mathrm{imax}-n}, \quad i \in (\mathrm{imax} - 1, \mathrm{imax}). \tag{24}$$

Second-order boundary schemes are used in the present study. Coefficients for the second-order boundary schemes at each left, near boundary point, 1 and 2 are $(a_{1,1}, a_{2,1}, a_{3,1}, a_{4,1}, a_{5,1}, a_{6,1}, \text{truncation error}) = \left(3, -14, 26, -24, 11, -2, \frac{17}{6} h^2 f^{(6)} \right)$ and $(a_{1,2}, a_{2,2}, a_{3,2}, a_{4,2}, a_{5,2}, a_{6,2}, \text{truncation error}) = \left(2, -9, 16, -14, 6, -1, \frac{5}{6} h^2 f^{(6)} \right)$. The right boundary formulas are obtained by

setting $a_{\text{imax}-n,i} = a_{n+1,\text{imax}-i+1}$ for $i \in (\text{imax} - 1, \text{imax})$. With regard to the C6 and E4, a second-order central scheme is used for point 3 and imax − 2. The user-specified constants are set to $C_\mu = 0.002$, $C_\beta = 1$, $C_\kappa = 0.01$, $C_D = 0.01$ and $C_Y = 100$. The effects of the constants C_D and C_Y for the newly proposed D_k^* are assessed in Section 3.1.4. These constants allows the scheme to capture discontinuities and not to introduce excessive dissipation for all the cases examined in this paper. Although the constants work well for wide range of test cases when $r = 4$ in Eqs. (17)–(20) and sixth-order compact/eighth-order filtering schemes are used, the constants will possibly need to be adjusted if different value of r or other numerical schemes are adopted.

The approximate truncated-Gaussian filter of Cook and Cabot [10] is applied to interior points sequentially along each grid line for the overbar in Eqs. (17)–(20):

$$\bar{f}_i = \frac{3565}{10,368}f_i + \frac{3091}{12,960}(f_{i-1} + f_{i+1}) + \frac{1997}{25,920}(f_{i-2} + f_{i+2}) + \frac{149}{12,960}(f_{i-3} + f_{i+3}) + \frac{107}{103,680}(f_{i-4} + f_{i+4}). \tag{25}$$

At the near boundary points, $1, \ldots, 4$ and $\text{imax} - 3, \ldots, \text{imax}$, for a non-periodic boundary such as a reflecting wall condition, the value f_i is mirrored across the boundary to apply Eq. (25).

2.4. Numerical scheme

The equations are solved in generalized curvilinear coordinates, where spatial derivatives for convective terms, viscous terms, metrics and Jacobian are evaluated by the sixth-order compact differencing scheme [1]. For any scalar quantity f, the finite difference approximation to the first and second spatial derivatives at node i, $\frac{\partial f_i}{\partial \xi_l}$ and $\frac{\partial^2 f_i}{\partial \xi_l^2}$ are obtained by the following formulas:

$$\alpha_1 \frac{\partial f_{i-1}}{\partial \xi_l} + \frac{\partial f_i}{\partial \xi_l} + \alpha_1 \frac{\partial f_{i+1}}{\partial \xi_l} = a_1 \frac{f_{i+1} - f_{i-1}}{2\Delta\xi_l} + b_1 \frac{f_{i+2} - f_{i-2}}{4\Delta\xi_l} \tag{26}$$

$$\alpha_2 \frac{\partial^2 f_{i-1}}{\partial \xi_l^2} + \frac{\partial^2 f_i}{\partial \xi_l^2} + \alpha_2 \frac{\partial^2 f_{i+1}}{\partial \xi_l^2} = a_2 \frac{f_{i+1} - 2f_i + f_{i-1}}{\Delta\xi_l^2} + b_2 \frac{f_{i+2} - 2f_i + f_{i-2}}{4\Delta\xi_l^2} \tag{27}$$

where $\alpha_1 = 1/3$, $a_1 = 14/9$ and $b_1 = 1/9$ and $\alpha_2 = 2/11$, $a_2 = 12/11$ and $b_2 = 3/11$ for the sixth-order schemes. Instead of applying the first derivative twice, the second derivative scheme is used for the viscous flux vectors reformulated in the non-conservative form and the original double Laplacians formulation of localized artificial diffusivity scheme. A fourth-order Runge–Kutta method is used for temporal integration.

The following eighth (2Nth)-order low-pass spatial filtering scheme [1] is used on the conservative properties once in each direction after each final Runge–Kutta step in order to ensure numerical stability:

$$\alpha_f \breve{f}_{i-1} + \breve{f}_i + \alpha_f \breve{f}_{i+1} = \sum_{n=0}^{N} \frac{a_n}{2}(f_{i+n} + f_{i-n}), \tag{28}$$

where f is the solution vector, and $\breve{f}$ is filtered quantity. A eighth-order filter is obtained with $a_0 = \frac{93+70\alpha_f}{128}$, $a_1 = \frac{7+18\alpha_f}{16}$, $a_2 = \frac{-7+14\alpha_f}{32}$, $a_3 = \frac{1-2\alpha_f}{16}$, $a_4 = \frac{-1+2\alpha_f}{128}$. The α_f is a free parameter satisfying the inequality $-0.5 < \alpha_f \leqslant 0.5$. In this range, as α_f is increased, a less suppression is realized. In the present study, the α_f is fixed to 0.495 for all the cases examined in this paper. High-order one-sided formulas are used for the near boundary points at $1, \ldots, 4$ and correspondingly at imax − 3, ..., imax [14]. Detailed spectral responses of these filters may be found in Ref. [15].

3. Numerical results

The numerical results with the original double Laplacians formulations of localized artificial diffusivity that are evaluated by using sixth-order compact differencing scheme are denoted LAD-C6 where the Δ scaling in Eqs. (11)–(14) is evaluated by the geometrically averaged grid spacing. The results from using the localized artificial diffusivity schemes for multi-dimensional generalized coordinate system (Eqs. (17)–(20)) are denoted LADG-C6, LADG-C4 and LADG-E4 where the last two characters such as C6, C4 and E4 denote the schemes used to evaluate the fourth derivatives in the equations: C6, sixth-order tridiagonal scheme; C4, fourth-order tridiagonal scheme; E4, fourth-order explicit scheme.

3.1. Performance of localized artificial diffusivity scheme in generalized form

Firstly, the performances of the localized artificial diffusivity scheme in generalized forms for smooth and non-smooth flows are evaluated through the simple problems of 2D vortex advection, stationary shock wave, contact discontinuity and material interface on isotropic and wavy meshes.

3.1.1. Two-dimensional vortex advection
The first test case is an inviscid convecting vortex in a uniform flow on isotropic Cartesian and wavy meshes introduced by Visbal and Gaitonde [2]. Since vortex preservation is sensitive to the numerical dissipation, this problem can be used to assess the impact of the generalized formulations of localized artificial diffusivity on the smooth flow.

The initial velocity and pressure field of the zero net circulation vortex is given by the following relations [16]:

$$u = U_\infty - \frac{C(y - y_c)}{R_c^2} \exp \frac{-r^2}{2}, \tag{29}$$

$$v = \frac{C(x - x_c)}{R_c^2} \exp \frac{-r^2}{2}, \tag{30}$$

$$p = p_\infty - \frac{\rho C^2}{2R_c^2} \exp(-r^2), \tag{31}$$

where u and v are the x and y velocity components, p is the static pressure, R_c is the vortex core radius and r^2 is defined as

$$r^2 = \frac{(x - x_c)^2 + (y - y_c)^2}{R_c^2}. \tag{32}$$

The uniform freestream Mach number, the non-dimensional vortex strength and center of the vortex are: $M_\infty = 0.1$, $C/(U_\infty R_c) = 0.02$ and $x_c = y_c = 0$. The density is assumed constant.

3.1.1.1. On uniform Cartesian meshes. Seven different levels of grid spacing $\Delta x/R_c = \Delta y/R_c = 1.5, 1.0, 0.8, 0.6, 0.4, 0.3$ and 0.2 are employed for the uniform Cartesian meshes. The wide range of grid resolution allows to investigate the error introduce by localized artificial diffusivity on the resolved and unresolved smooth flows. The computational domain is $-6 \leqslant x/R_c \leqslant 18$ and $-6 \leqslant y/R_c \leqslant 6$. Fig. 1 shows the computational grid ($\Delta x/R_c = \Delta y/R_c = 0.4$) and the initial vorticity contours. The computational time-step size is set to $\Delta t U_\infty/R_c = 0.002$ that corresponds to a Courant–Friedrichs–Lewy (CFL) number of 0.01 on the finest mesh. The results are discussed at times of $t U_\infty/R_c = 8$ and 80 where the vortex convects distances of $8R_c$ and $80R_c$. Periodic boundary conditions are applied on the boundaries in the x- and y-direction. For the $80R_c$ advection case, the vortex passes through the periodic boundary in the x-direction three times and reaches $x/R_c = 8$ at the instant of $t U_\infty/R_c = 80$.

Fig. 2 shows the comparison between the exact solution and the numerical simulations (without LADG, LADG-C6, -C4 and -E4) for the non-dimensionalized v-velocity v/U_∞ profiles along a horizontal centerline that passes through the vortex center. The results are obtained at time of $t U_\infty/R_c = 80$ on the Cartesian mesh with $\Delta x/R_c = \Delta y/R_c = 0.3$. All the results are nearly identical and in excellent agreement with the exact solution. The normalized L_∞-error norm in the v-velocity profile in terms of grid spacing is shown in Fig. 3. An estimation of the order of accuracy is also included in the figure (in parentheses) by using linear least-square fits to the data at $\Delta x/R_c = 0.4, 0.3$ and 0.2 obtained by the LADG-C6. As expected, the longer distance of the vortex convection introduces higher error. However, the error decreases consistently in both the short- and long-convection cases when the vortex is reasonably resolved. The errors obtained by the LADG methods almost exactly match with the error of the pure compact differencing scheme (without LADG) even if the vortex is not well resolved. The results indicate that the LADG methods does not show any major detrimental effect on the smooth flow even if the vortex is not well resolved by the compact differencing scheme on a given mesh. That is, the error introduced by the LADG methods on the smooth flow is always lower than the error from compact and filtering schemes.

3.1.1.2. On wavy meshes. Seven different levels of grid spacing, $\Delta x_0/R_c = \Delta y_0/R_c = 1.5, 1.0, 0.8, 0.6, 0.4, 0.3$ and 0.2 are employed for the vortex advection on the wavy meshes. The curvilinear mesh is analytically generated by the following formula [14]:

$$x_{i,j} = x_{\min} + \Delta x_0 \left[(i - 1) + A_x \sin \frac{n_x \pi (j - 1) \Delta y_0}{L_y} \right], \tag{33}$$

$$y_{i,j} = y_{\min} + \Delta y_0 \left[(j - 1) + A_y \sin \frac{n_y \pi (i - 1) \Delta x_0}{L_x} \right], \tag{34}$$
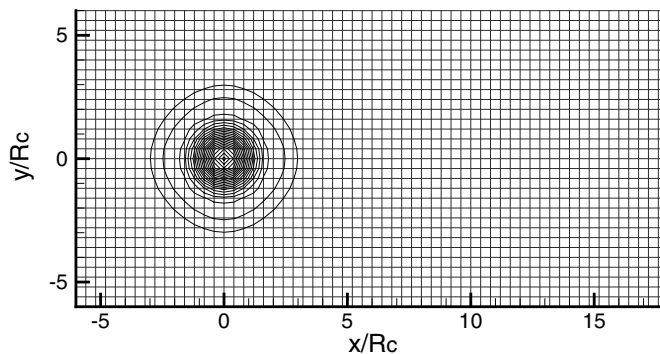

Fig. 1. Computational grid with $\Delta x/R_c = \Delta y/R_c = 0.4$ and the initial flow field of the vortex. Vorticity $\omega R_c/U_\infty$, 20 equally spaced contours from -0.004 to 0.036.
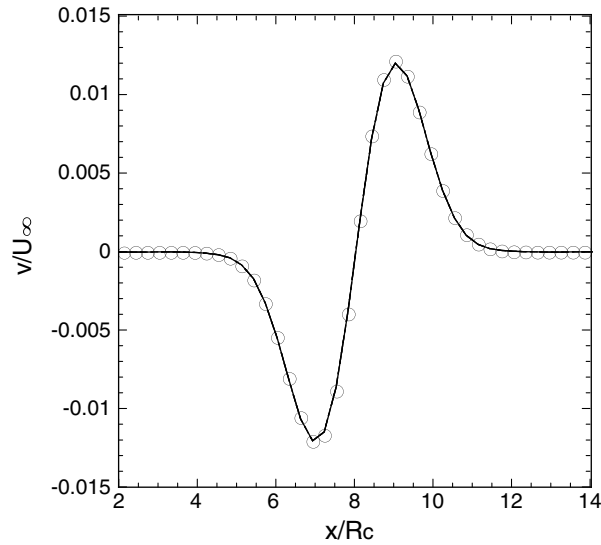
Fig. 2. Comparison of the non-dimensionalized v-velocity v/U_∞ profiles along centerline at the instant of $tU_\infty/R_c = 80$ on the uniform Cartesian mesh with $\Delta x/R_c = \Delta y/R_c = 0.3$. Circle, exact; solid line, without LADG; dashed line, LADG-C6; dashed-dot line, LADG-C4; dotted line, LADG-E4.
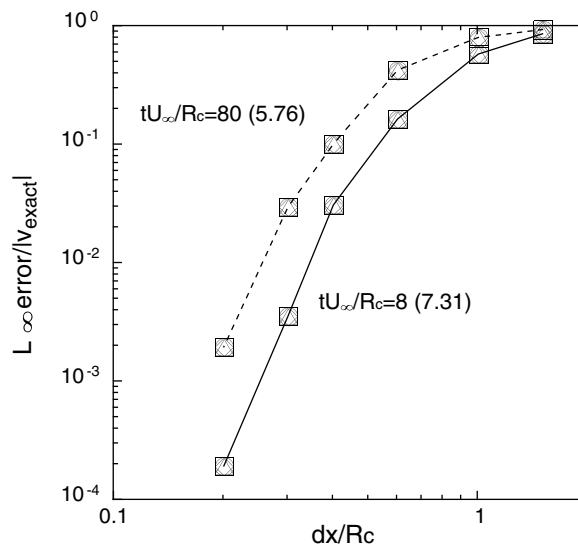

Fig. 3. Normalized L_∞-error norm in the v-velocity profile in terms of grid spacing on a uniform Cartesian mesh. Solid line, $tU_\infty/R_c = 8$; dashed line, $tU_\infty/R_c = 80$. Diamond, without LADG; circle, LADG-C6; square, LADG-C4; triangle, LADG-E4.

where the parameters are set to $x_{min} = y_{min} = -6$, $L_x = 24$, $L_y = 12$, $n_x = 2$, $n_y = 4$. A_x and A_y vary with the $\Delta x_0/R_c$ and $\Delta y_0/R_c$ to keep the same amplification of waviness: $A_x = 0.4R_c/\Delta x_0$ and $A_y = 1.6R_c/\Delta y_0$. Fig. 4 shows the computational grid ($\Delta x_0/R_c = \Delta y_0/R_c = 0.4$) and the initial vorticity contours. Same as the Cartesian case, the computational time-step size is set to $\Delta tU_\infty/R_c = 0.002$ and the results discussed are at the instants of $tU_\infty/R_c = 8$ and 80.

Fig. 5 shows the comparison between the exact solution and the numerical simulations for the v-velocity v/U_∞ along a j-constant line that passes through the vortex center. The results are obtained at the instant of $tU_\infty/R_c = 80$ on the wavy mesh with $\Delta x_0/R_c = \Delta y_0/R_c = 0.3$. The normalized L_∞-error norm in the v-velocity profile in terms of grid spacing is shown in Fig. 6. Similarly to the Cartesian grid case, the LADG methods on the wavy mesh does not show major impact both the well-resolved and unresolved smooth flows. All the results are nearly identical and the error decreases consistently in both the short- and long-convection cases.
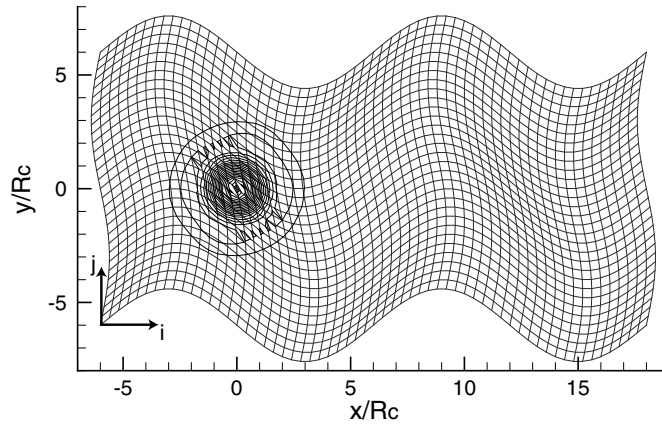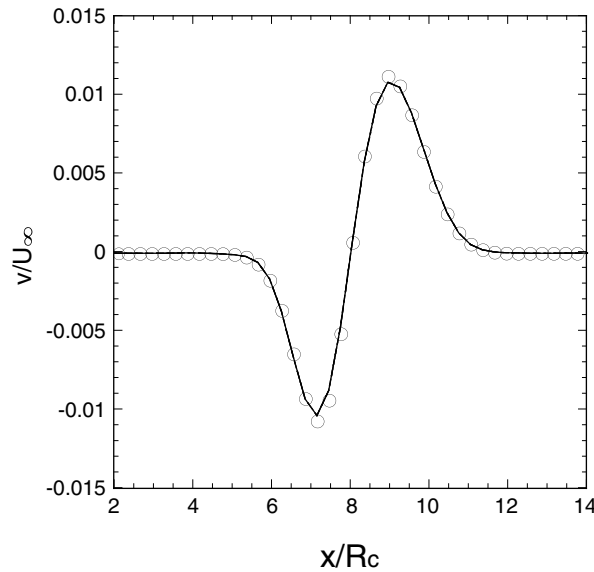
Fig. 4. Computational grid with $\Delta x_0/R_c = \Delta y_0/R_c = 0.4$ and the initial flow field of the vortex. Vorticity $\omega R_c/U_\infty$, 20 equally spaced contours from -0.004 to 0.036.

Fig. 5. Comparison of the non-dimensionalized v-velocity v/U_∞ profiles along a j-constant line that passes through the vortex center at the instant of $tU_\infty/R_c = 80$ on the wavy mesh with $\Delta x_0/R_c = \Delta y_0/R_c = 0.3$. Circle, exact; solid line, without LADG; dashed line, LADG-C6; dashed-dot line, LADG-C4; dotted line, LADG-E4.

3.1.2. Stationary normal shock wave

The second test case is a Mach 2 stationary normal shock wave that corresponds to a pressure jump $p_r/p_l = 4.5$ on 2D isotropic and wavy meshes, where the r and l subscripts denote the post- and pre-shock conditions. Performance of the generalized formulations of localized artificial diffusivity, μ^* and β^*, to capture the shock wave is investigated through the problem. κ^* and D^* are turned off ($\kappa^* = D^* = 0$) in this test case. The initial conditions satisfy the Rankine–Hugoniot solution. Three different levels of mesh size $\Delta x = \Delta y = 0.02$, 0.01 and 0.005 are employed for both the isotropic Cartesian and wavy meshes. The computational domain for the isotropic Cartesian mesh extends $-0.5 \leqslant x \leqslant 0.5$. The wavy meshes are generated in the same manner as the previous vortex advection case, but with $x_{min} = -0.5$, $y_{min} = 0$, $L_x = 1$, $L_y = 0.5$. Periodic boundary conditions are applied along the boundaries in the j-direction. Since the normal shock wave is not aligned with the wavy mesh, this problem can also be used to assess the impact of the cross-derivative terms, which are neglected in Eqs. (17) and (18), on the results.

Fig. 7 shows the converged pressure profiles across the stationary shock wave obtained by the LADG-C6 with the three different levels of mesh size. The profiles on the 2D wavy mesh are along a j-constant centerline. The results of the LADG-C4 and LADG-E4 are almost identical to the LADG-C6 (not shown here). Maximum wiggles amplitude and numerical shock
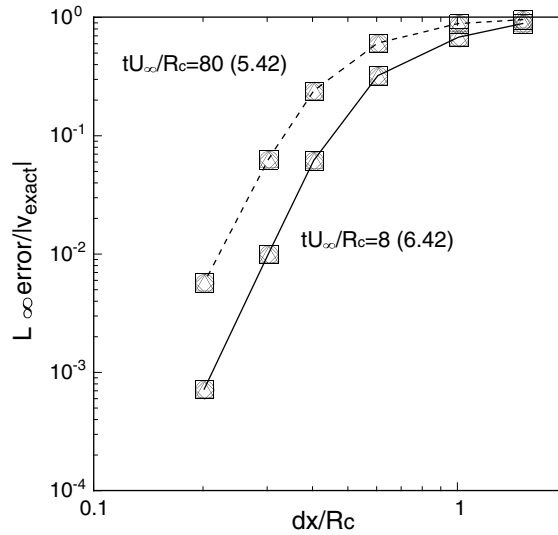
Fig. 6. Normalized L_∞-error norm in the v-velocity profile in terms of grid spacing on a wavy mesh. Solid line, $tU_\infty/R_c = 8$; dashed line, $tU_\infty/R_c = 80$. Diamond, without LADG; circle, LADG-C6; square, LADG-C4; triangle, LADG-E4.
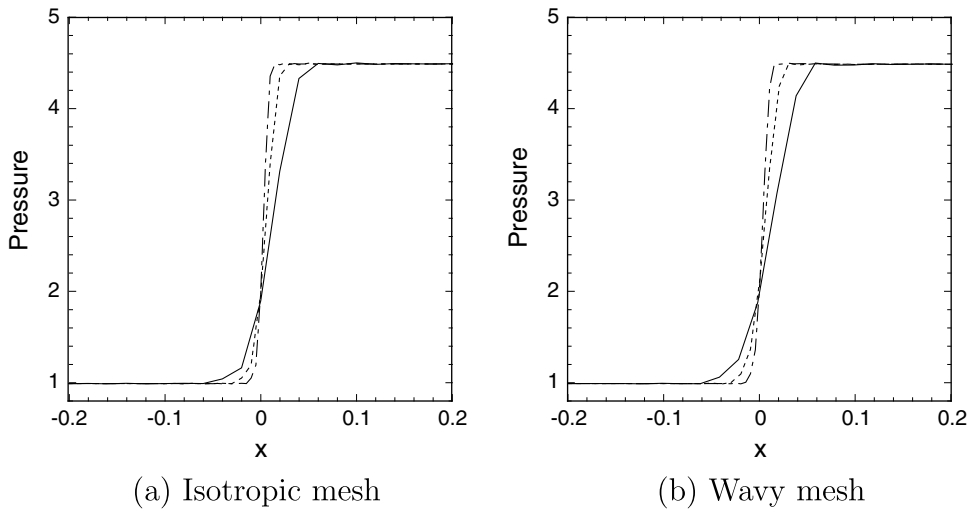

Fig. 7. Pressure profiles across the stationary shock wave obtained by LADG-C6 with the three different levels of mesh size $\Delta x = \Delta y = 0.02$, 0.01 and 0.005. Solid line, $\Delta x = 0.02$; dashed line, $\Delta x = 0.01$; dashed-dot line, $\Delta x = 0.005$.

thickness in terms of grid spacing are shown in Figs. 8 and 9. The wiggles amplitude is normalized by the pressure jump across the shock wave $\Delta p = p_r - p_l$ and the numerical shock thickness is defined by [12]

$$\frac{\delta}{\Delta x} = \frac{\Delta p}{\Delta x \frac{\partial p}{\partial x}\big|_{\max}}. \tag{35}$$

The stationary shock wave is captured well without significant wiggles by smearing the shock discontinuity. The shock maintains perfectly 1D shock structure on the Cartesian meshes and almost 1D on the wavy meshes. Maximum v-velocity component in the computational domain is 0 on the Cartesian meshes and 1.2%, 1.0% and 0.66% of the Mach 2 freestream u-velocity on the wavy meshes with the mesh sizes $\Delta x = \Delta y = 0.02$, 0.01 and 0.005, respectively. As the mesh size is refined, the shock discontinuity is sharpened in the physical space and the result converges to the exact solution. All the generalized formulations maintain the wiggles amplitude below 0.5% both on the isotropic and wavy meshes. The numerical shock thickness is relatively insensitive to the grid resolution. The shock is captured approximately over the same number of grid points even when the grid resolution is changed. Similar characteristics are also obtained by the 1D formulation of artificial non-
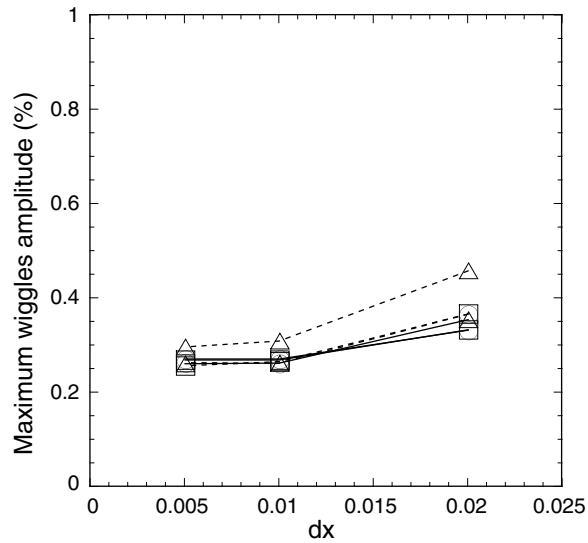
Fig. 8. Non-dimensionalized maximum wiggles amplitude in % in terms of grid spacing for the stationary shock wave. Solid line, isotropic mesh; dashed line, wavy mesh. Circle, LADG-C6; square, LADG-C4; triangle, LADG-E4.
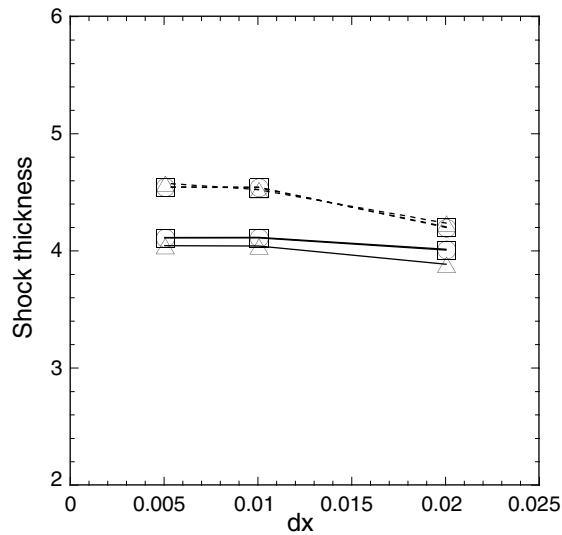

Fig. 9. Non-dimensionalized numerical shock thickness in terms of grid spacing for the stationary shock wave. Solid line, isotropic mesh; dashed line, wavy mesh. Circle, LADG-C6; square, LADG-C4; triangle, LADG-E4.

linear diffusivity scheme for a 1D isotropic mesh [12]. The shock simulated on the wavy mesh is slightly more smeared than that on the Cartesian mesh. However, 97% of the pressure jump across the shock wave is captured over six grid points in both the meshes. Since most of the error is introduced by smearing the shock wave over the fixed number of grid points, the $L1$-error in the region of shock wave decreases as first-order with increasing the grid resolution. The degradation of accuracy of the numerical scheme to the first-order near shock wave is the best we can achieve and same as other shock-capturing schemes.

3.1.3. Stationary contact discontinuity

The third test case is a strong temperature discontinuity at a stationary contact surface that corresponds to a temperature jump $T_r/T_l = 10$ on 2D isotropic and wavy meshes. Performance of κ^* in Eq. (19) to capture the contact discontinuity on isotropic and wavy meshes is investigated through the problem. μ^*, β^* and D^* are turned off ($\mu^* = \beta^* = D^* = 0$) in this test case.

Initial left- and right-side conditions for an inviscid fluid are: $\rho_l = 1.0$ for $x \leqslant 0$ and $\rho_r = 0.1$ for $x > 0$ with $\boldsymbol{u} = 0.0$ and $p = 1.0$. The same 2D isotropic and wavy meshes with three different levels of resolution as in Section 3.1.2 are used. Periodic boundary conditions are applied along the boundaries in the j-direction.

Figs. 10 and 11 show maximum wiggles amplitude and numerical contact surface thickness in terms of grid spacing. All results reach almost a steady state and κ^* essentially turns off once the interface is smeared over a numerically resolvable scale. That is, a contact discontinuity with nearly fixed thickness is obtained (the discontinuity spreads less than 0.1% of the numerical contact surface thickness over thousands time-steps). The wiggles amplitude is normalized by the temperature jump across the shock wave $\Delta T = T_r - T_l$ and the non-dimensionalized numerical contact thickness is defined by

$$\frac{\delta}{\Delta x} = \frac{\Delta T}{\Delta x \frac{\partial T}{\partial x}\big|_{\max}}. \tag{36}$$

Basically, the results are qualitatively similar to the stationary shock wave case. The temperature discontinuity is captured by smearing the contact discontinuity over the approximately fixed number of grid points. That is, the numerical accuracy in the $L1$-error near contact discontinuity is first-order. All the LADG methods maintain the wiggles amplitude below 0.5% both on the isotropic and wavy meshes. The contact discontinuity simulated on the wavy mesh is slightly more smeared than that on the Cartesian mesh.

3.1.4. Stationary material interface

The last test case for the performance evaluation of the localized artificial diffusivity scheme is a mass fraction discontinuity at the stationary material interface on 2D isotropic and wavy meshes. Performance of D_k^* in Eq. (20) to capture the material interface on isotropic and wavy meshes is investigated. μ^*, β^* and κ^* are turned off ($\mu^* = \beta^* = \kappa^* = 0$) in this test case. Initial left- and right-side conditions for an inviscid fluid are: $Y_l = 0.0$ for $x \leqslant 0$ and $Y_r = 1.0$ for $x > 0$ with $\rho = 1.0$, $\boldsymbol{u} = 0.0$ and $p = 1.0$. Periodic boundary conditions are applied along the boundaries in the j-direction.

Because the proposed D_k^* model is different from the original model, we first investigate the effect of user-specified constants C_D and C_Y for the proposed D_k^* in order to set a proper value of the constants. The LADG-C6 method with the isotropic Cartesian mesh ($\Delta x = \Delta y = 0.02$) is used for this discussion. The first term in the model for D_k^* is the main artificial diffusivity term and the second term is only activated in the region where the mass fraction exceeds the bound of $0 \leqslant Y \leqslant 1$. The second term acts to restore the mass fraction within the admissible bounds. The effect of the C_D is investigated first without the second term by setting $C_Y = 0$. In Fig. 12, maximum wiggles amplitude is plotted on the left axis with solid line with circle and numerical material interface thickness is plotted on the right axis with dashed line with triangle in terms of C_D ranging between 0 and 0.05. Non-dimensionalized numerical material interface thickness is defined by

$$\frac{\delta}{\Delta x} = \frac{\Delta Y}{\Delta x \frac{\partial Y}{\partial x}\big|_{\max}}, \text{ where } \Delta Y_r - Y_l. \tag{37}$$

There is a clear trade-off between the wiggles amplitude and material interface thickness. That is, as C_D increases, the material discontinuity is smeared and the amplitude of the spurious oscillations decreases. For $C_D = 0.01$, 97% of the mass fraction
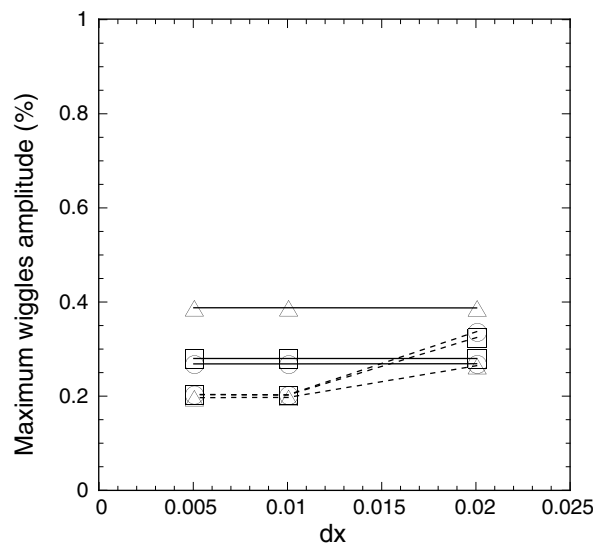

Fig. 10. Non-dimensionalized maximum wiggles amplitude in % in terms of grid spacing for the stationary contact discontinuity. Solid line, isotropic mesh; dashed line, wavy mesh. Circle, LADG-C6; square, LADG-C4; triangle, LADG-E4.
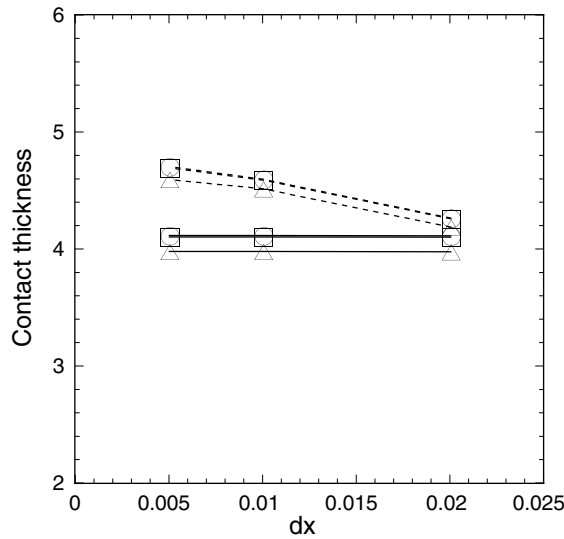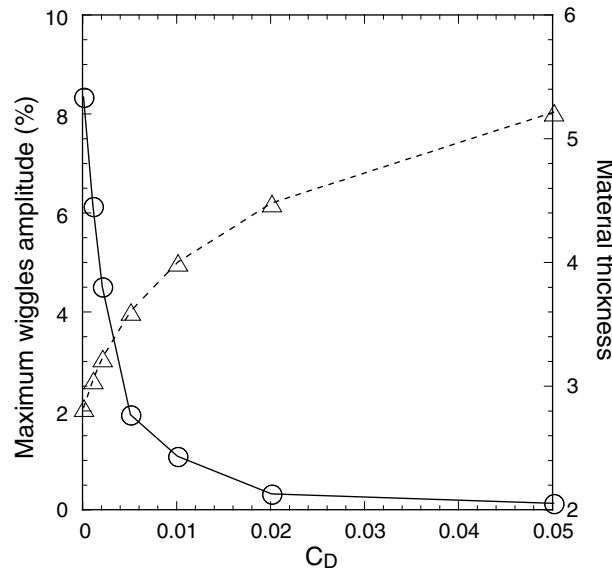
Fig. 11. Non-dimensionalized numerical contact surface thickness in terms of grid spacing for the stationary contact discontinuity. Solid line, isotropic mesh; dashed line, wavy mesh. Circle, LADG-C6; square, LADG-C4; triangle, LADG-E4.

Fig. 12. Maximum wiggles amplitude in % plotted on left axis with solid line with circle and non-dimensionalized numerical material interface thickness plotted on right axis with dashed line with triangle in terms of C_D with fixed $C_Y = 0$ for the stationary material interface.

jump across the interface is captured over six grid points that is comparable to the capability of the shock and contact discontinuity capturing and the maximum wiggles amplitude is approximately 1.1%.

With fixed $C_D = 0.01$, Fig. 13 shows maximum bounds ($0 \leqslant Y \leqslant 1$) exceeded and numerical material interface thickness in terms of C_Y. Logarithm scale is used in the left axis. As expected, the second term in D_k^* is effective in keeping mass fractions between 0 and 1 almost without affecting the interface thickness. With the set of $C_D = 0.01$ and $C_Y = 100$, the mass fraction almost keeps the bounds of $0 \leqslant Y \leqslant 1$ and also the interface is captured without introducing excessive dissipation. The fixed constants of $C_D = 0.01$ and $C_Y = 100$ are used for all the test cases discussed in the rest of the paper.

Figs. 14 and 15 show maximum wiggles amplitude and numerical material interface thickness in terms of grid spacing. The same 2D isotropic Cartesian and wavy meshes in Section 3.1.2 are used for this discussion. All results reach almost a steady state with nearly constant material interface thickness (the interface spreads less than 0.05% of its thickness over
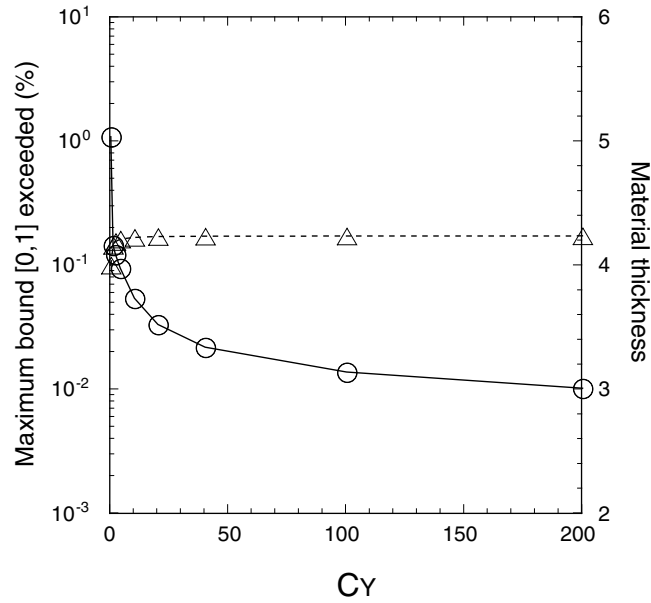
Fig. 13. Maximum bound ($0 \leqslant Y \leqslant 1$) exceeded in % plotted on left axis with solid line with circle and non-dimensionalized numerical material interface thickness plotted on right axis with dashed line with triangle in terms of C_Y with fixed $C_D = 0.01$ for the stationary material interface.
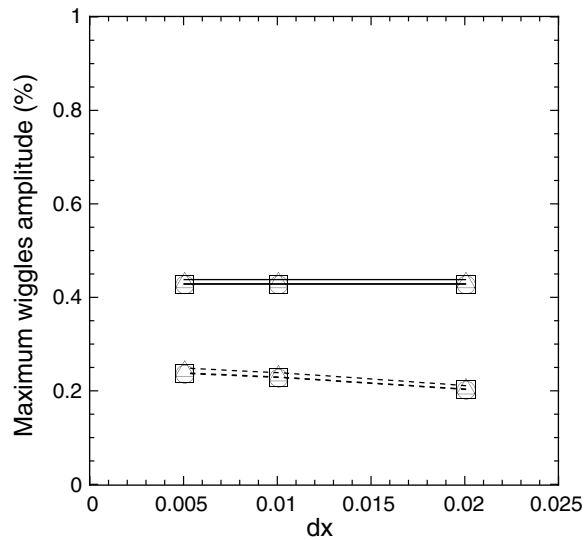

Fig. 14. Maximum wiggles amplitude in % in terms of grid spacing for the stationary material interface. Solid line, isotropic mesh; dashed line, wavy mesh. Circle, LADG-C6; square, LADG-C4; triangle, LADG-E4.

thousands time-steps). The results are qualitatively similar to the stationary shock wave and contact discontinuity cases. The model smears the material interface over the fixed number of grid points without significant wiggles on both the isotropic Cartesian and wavy meshes.

Analysis of the results for smooth and non-smooth flows indicates that the proposed localized artificial diffusivity scheme successfully captures the discontinuities with minimal effects by smearing the discontinuities on both the isotropic Cartesian and wavy meshes and does not show major impact on both the well-resolved and unresolved smooth flows. The amplitude of wiggles near the discontinuity and the number of grid points to capture the discontinuity do not depend on the mesh size. The simplification of the method in which all the cross-derivative terms are neglected does not show any major detrimental effect on both smooth and non-smooth flows.
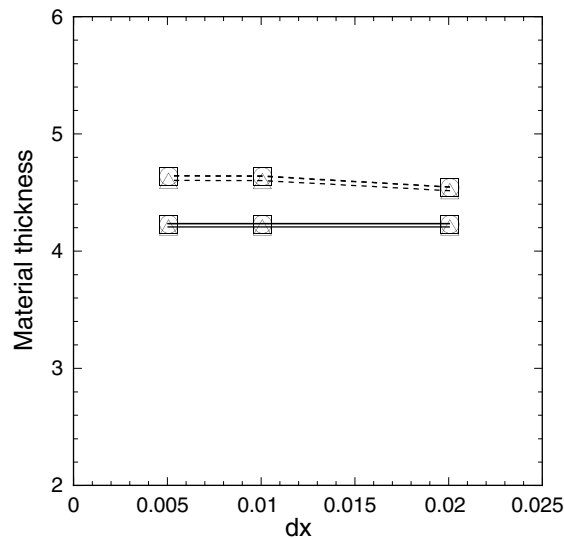
Fig. 15. Non-dimensionalized numerical material interface thickness in terms of grid spacing for the stationary material interface. Solid line, isotropic mesh; dashed line, wavy mesh. Circle, LADG-C6; square, LADG-C4; triangle, LADG-E4.

3.2. One-dimensional Sod and Lax shock tube problems

The 1D shock tube problems introduced by Sod [17] and Lax [18] are used to investigate the capability of the localized artificial diffusivity scheme on 1D moving shock and contact discontinuities. Initial left- and right-side conditions for Sod shock tube problem are: $\rho_l = 1.0$, $u_l = 0.0$ and $p_l = 1.0$ for $x \leqslant 0$, and $\rho_r = 0.125$, $u_r = 0.0$ and $p_r = 0.1$ for $x > 0$. The conditions for Lax shock tube problem are: $\rho_l = 0.445$, $u_l = 0.698$ and $p_l = 3.528$ for $x \leqslant 0$, and $\rho_r = 0.5$, $u_r = 0.0$ and $p_r = 0.571$ for $x > 0$. Firstly, simulations are performed on a uniformly spaced grid with 201 grid points in the region of $-0.5 \leqslant x \leqslant 0.5$ ($\Delta x = 0.005$). Then, the results obtained by a 2D anisotropic mesh with an aspect ratio of 5 ($\Delta y = 5\Delta x$) are discussed. The anisotropic Cartesian mesh consists of 201 and 13 grid points in the x- and y-direction where $\Delta x = 0.005$ and $\Delta y = 0.025$. The test cases of an anisotropic mesh is used to confirm the consistency between the original 1D formulation and the generalized model on a multi-dimensional formulation. Periodic boundary conditions are applied on the boundaries in the y-direction.

3.2.1. On an isotropic mesh

Fig. 16 shows the comparison between the exact solution, the original localized artificial diffusivity method LAD-C6, and the generalized methods LADG-C6, LADG-C4 and LADG-E4 for the density, the artificial viscosity and thermal conductivity at the time of $t = 0.2$ for Sod problem and $t = 0.13$ for Lax problem on an isotropic mesh. The artificial viscosity and thermal conductivity are normalized by the maximum obtained by LAD-C6. The shock and contact discontinuities are captured well without significant spurious oscillations and show good agreement with the exact solution. The artificial viscosity and diffusivity are automatically localized near the shock and contact discontinuities. Ninety-seven percentages of the density jumps across the shock and contact discontinuities are captured over five and six grid points in both the cases, respectively. Although slight wiggles appear near the discontinuities, maximum wiggles amplitudes in the density normalized by the density jump are 2.0% for Sod problem and 1.3% for Lax problem. The LAD-C6, LADG-C6, LADG-C4 and LADG-E4 show almost identical results as expected. The artificial viscosities and conductivities obtained by the LAD-C6, LADG-C6 and LADG-C4 are also nearly identical. The LADG-E4 shows slightly lower artificial viscosity and conductivity than the other schemes but the spatial extent is similar. Overall, there is no significant difference in the performance of the schemes.

3.2.2. On an anisotropic mesh

Fig. 17 shows the comparison between the exact solution and the numerical simulations at the time $t = 0.2$ for Sod problem and $t = 0.13$ for Lax problem on an anisotropic mesh. The artificial viscosity and thermal conductivity are normalized by using the same maximum values obtained by LAD-C6 in the first test case 3.2.1. The LAD-C6, which uses geometrically averaged grid spacing for the Δ scaling, introduces excessive artificial dissipation at the discontinuity. The excessive viscosity and conductivity causes overly smeared shock and contact discontinuities and expansion waves. Also, in the Sod problem, proper post-shock and -contact conditions are not recovered. These are due to the undesirable effects from the geometrically averaged grid spacing. On the other hand, the multi-dimensional formulations work well to consistently maintain the original properties of the 1D formulation. The results of LADG-C6, LADG-C4 and LADG-E4 match with the results obtained in the first test case on the 1D isotropic mesh.
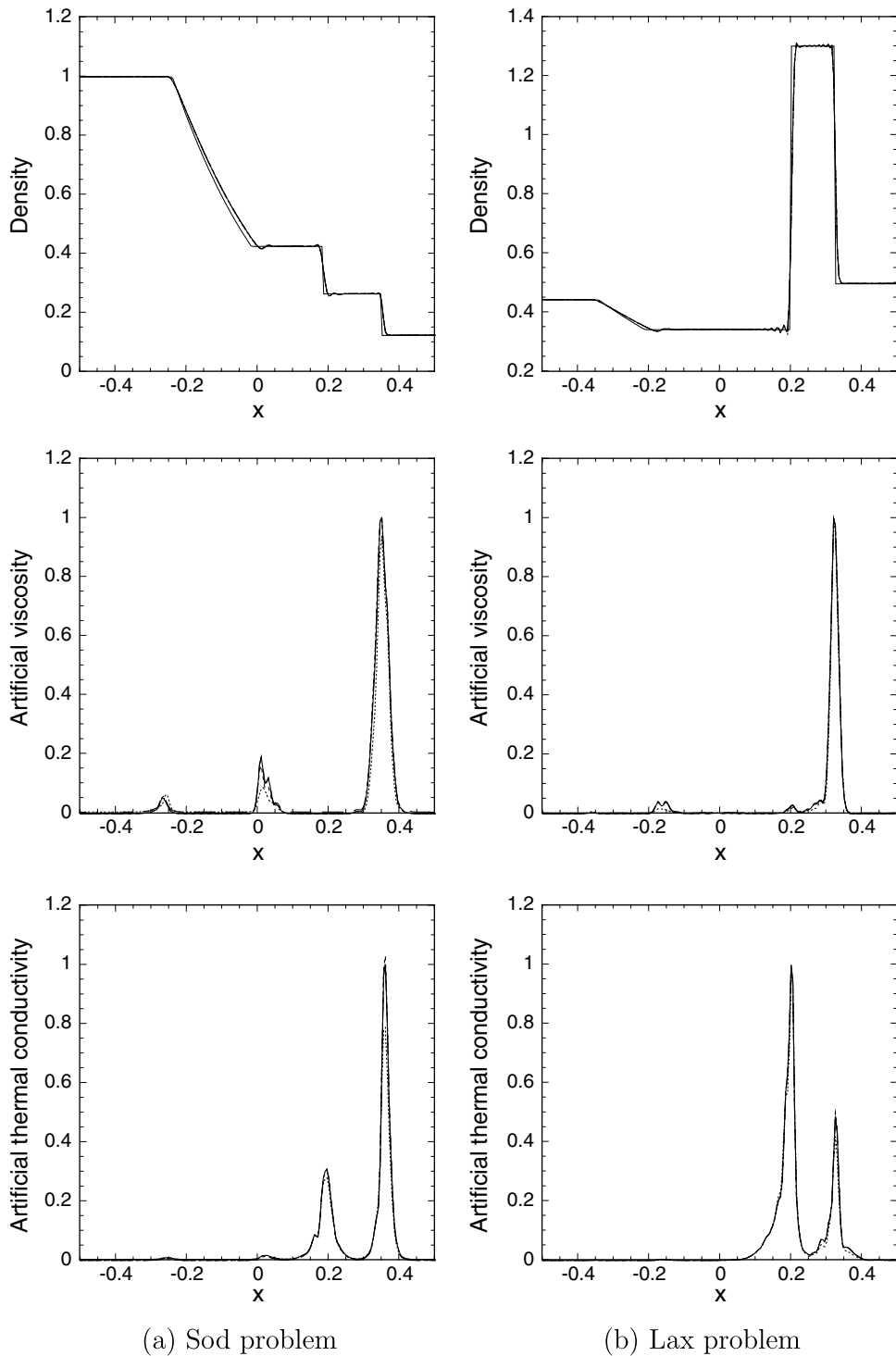
(a) Sod problem	(b) Lax problem

Fig. 16. Numerical simulations of the 1D Sod and Lax shock tube problems on an isotropic mesh with $\Delta x = 0.005$. Density, normalized artificial viscosity and thermal conductivity are presented at $t = 0.2$ for Sod problem and $t = 0.13$ for Lax problem. Thin solid line, exact; thick solid line, LAD-C6; dashed line, LADG-C6; dashed-dot line, LADG-C4; dotted line, LADG-E4.

3.3. One-dimensional Shu–Osher problem

The 1D shock–entropy wave interaction introduced by Shu and Osher [6] is investigated to assess the capability of the generalized formulation of localized artificial diffusivity scheme on shock–turbulence interaction. Because the entropy
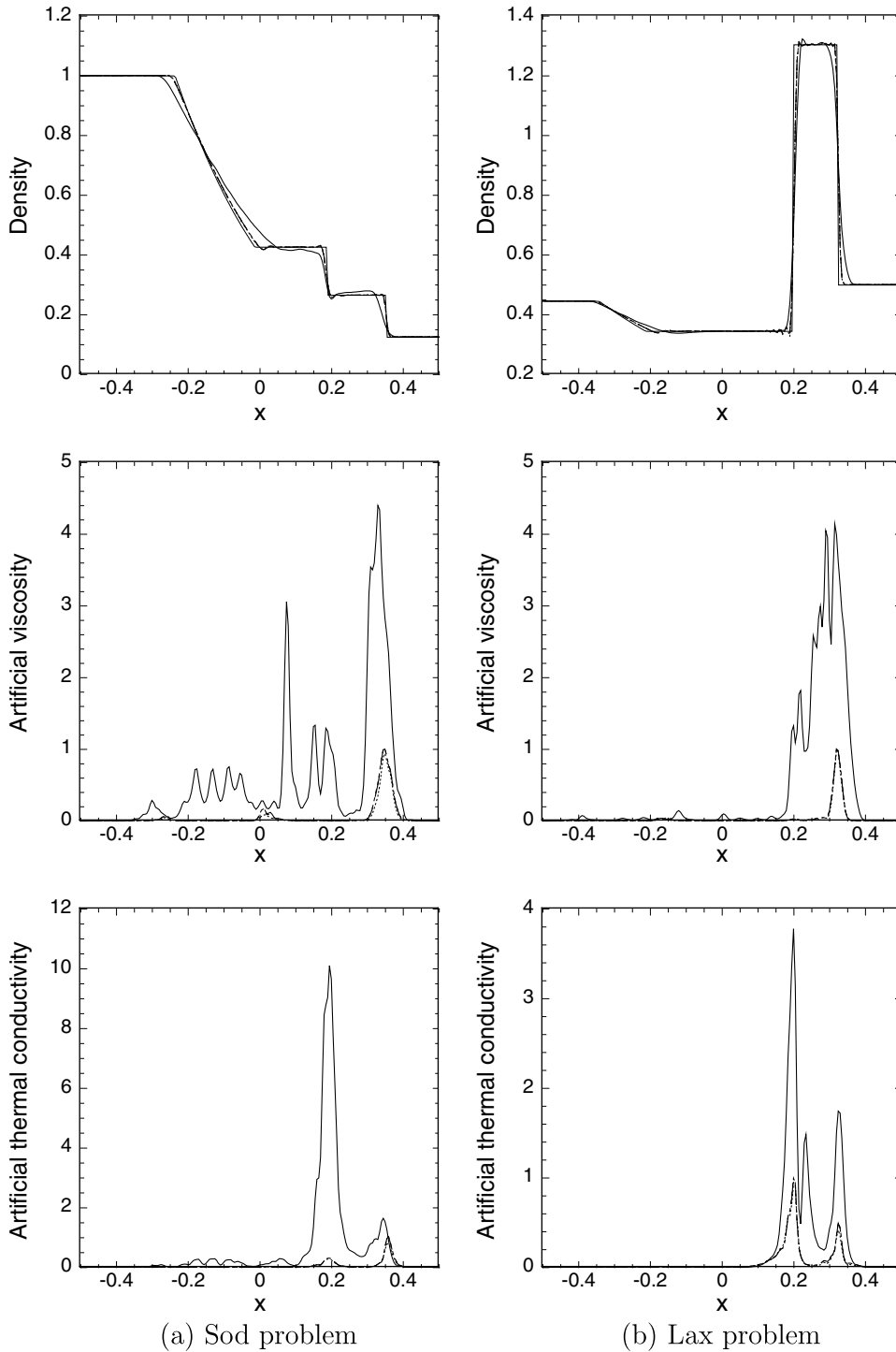
Fig. 17. Numerical simulations of the 1D Sod and Lax shock tube problems on a 2D mesh with a mesh aspect ratio of 5 (5$\Delta x = \Delta y$, $\Delta x = 0.005$). Density, artificial viscosity and thermal conductivity are presented at $t = 0.2$ for Sod problem and $t = 0.13$ for Lax problem. Thin solid line, exact; thick solid line, LAD-C6; dashed line, LADG-C6; dashed-dot line, LADG-C4; dotted line, LADG-E4.

waves are sensitive to the numerical dissipation, schemes using an upwinding to capture discontinuities usually introduce excessive numerical dissipation and the entropy waves are damped. Initial left- and right-side conditions are: $\rho_l = 3.857143$, $u_l = 2.629369$ and $p_l = 10.33333$ for $x < -4$, and $\rho_r = 1 + 0.2\sin(5x)$, $u_r = 0.0$ and $p_r = 1.0$ for $x \geqslant -4$. Simulations are performed on a uniformly spaced grid with 201 grid points where the computational domain is $-5 \leqslant x \leqslant 5$ with $\Delta x = 0.05$.
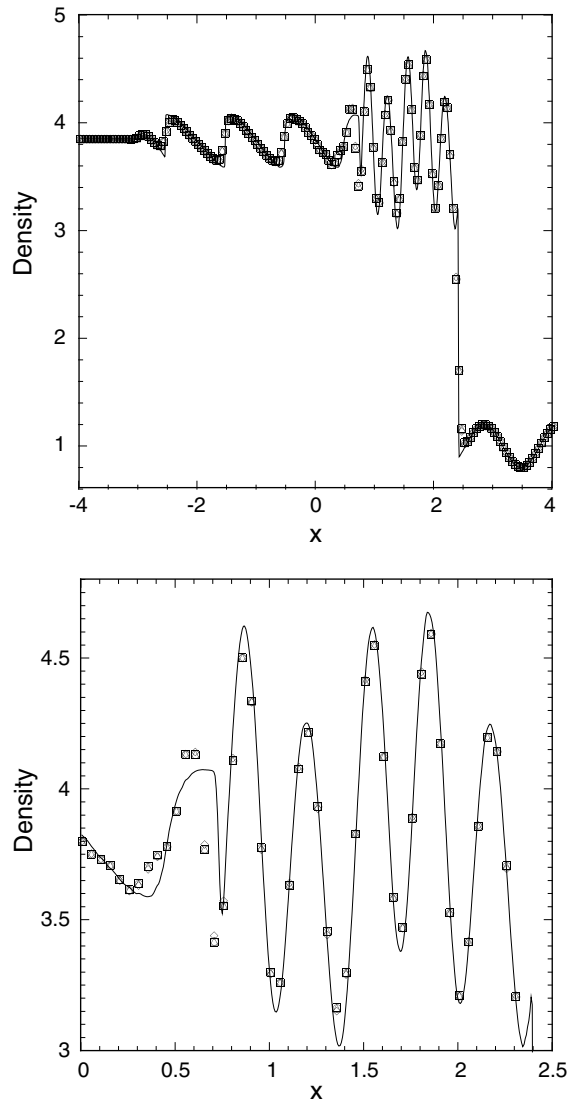
Fig. 18. Numerical simulations of the 1D Shu–Osher shock–turbulence interaction with Δx = 0.05. Density is presented at t = 1.8. Thin solid line, reference solution obtained on 1601 grid points with ninth-order WCNS scheme [19]; circle, LAD-C6; square, LADG-C6; triangle, LADG-C4; diamond, LADG-E4 (almost identical each other).

Fig. 18 shows the comparison between the reference solution and the numerical simulations for the density at the time of t = 1.8. The reference solution is obtained on 1601 grid points with ninth-order weighted compact non-linear scheme (WCNS) [19]. Numerical simulations of the original and all the generalized formulations capture the shock wave and also simultaneously resolve the entropy waves well. The LAD-C6, LADG-C6, LADG-C4 and LADG-E4 show almost identical density distributions and reasonable agreement with the reference solution.

### 3.4. Comparison of numerical schemes on 1D shock-related problems

It is useful to understand the advantages and disadvantages of the proposed LADG method by comparing with other high-order shock-capturing schemes. One-dimensional Sod and Lax shock tube and Shu–Osher shock–entropy wave interaction problems are used to compare the LADG scheme, seventh- and ninth-order weighted ENO (WENO) scheme [20] and WCNS [19,21]. A Roe-type characteristic-wise finite difference WENO is used for the flux evaluation in the WENO. Monotonicity preserving limiters are not used. Seventh- and ninth-order WENO use 9 and 11 points in the stencil to evaluate a first spatial derivative at a node and require higher computational cost than the compact scheme with LADG method. In the WCNS, characteristic variables are used for the interpolation scheme and the flux at the cell interface is evaluated by Roe's flux difference splitting. Seventh- and ninth-order WCNS require higher computational cost than the WENO and use 17 and 21 points in the

stencil to evaluate a first derivative. The seventh- and ninth-order WENO and WCNS are denoted WENO7, WENO9, WCNS7 and WCNS9. The WENO and WCNS data discussed here are provided by Dr. E. Johnsen and Dr. T. Nonomura. The numerical setup for the simulations is the same as in Sections 3.2.1 and 3.3.
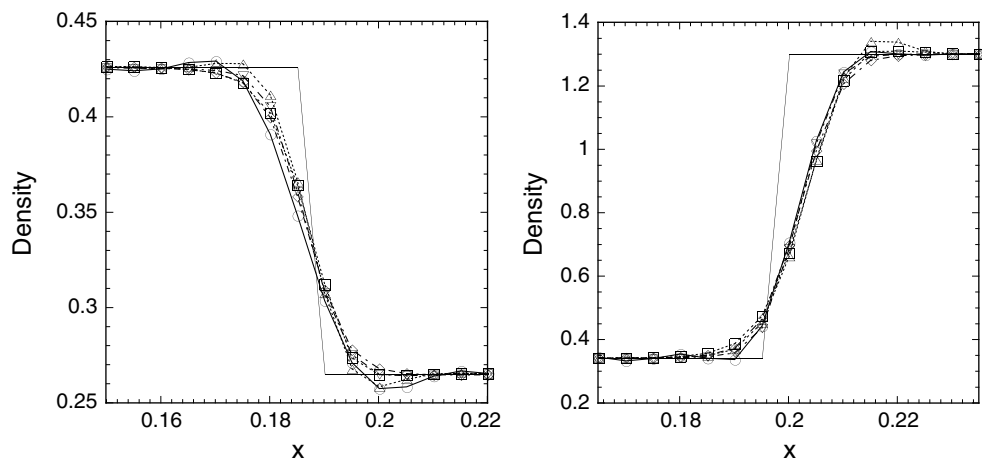
Comparison between the numerical methods for the density of 1D Sod and Lax problems at the time of $t = 0.2$ for Sod problem and $t = 0.13$ for Lax problem is shown in Fig. 19. Close-up views near the shock and contact discontinuity regions are presented. Table 1 summarizes the comparison of the numerical discontinuity thickness and maximum wiggles at the post- and pre-shock and contact discontinuity regions. The result of a ninth-order monotonicity preserving WENO (MPWE-NO) [20] is also included in Lax shock tube problem. The wiggles amplitude is normalized by the density jump across the shock and contact discontinuities, and the numerical shock and contact thicknesses are defined by

$$\frac{\delta}{\Delta x} = \frac{\Delta \rho}{\Delta x \frac{\partial \rho}{\partial x}\big|_{\max}}. \tag{38}$$

Basically, the LADG-C6 method shows slightly more smeared shock and contact discontinuities compared with the high-order WENO and WCNS except at the contact discontinuity for Lax problem where similar contact thickness is obtained by both the LADG-C6 and ninth-order WENO/WCNS. The maximum differences of the discontinuity thickness in Eq. (38) between the LADG-C6 and WENO/WCNS are 0.68 and 0.57 grid points at the shock and contact discontinuity regions, respectively, compared with the WCNS9 and WENO9. Although the wiggles amplitude obtained by the LADG-C6 is basically larger
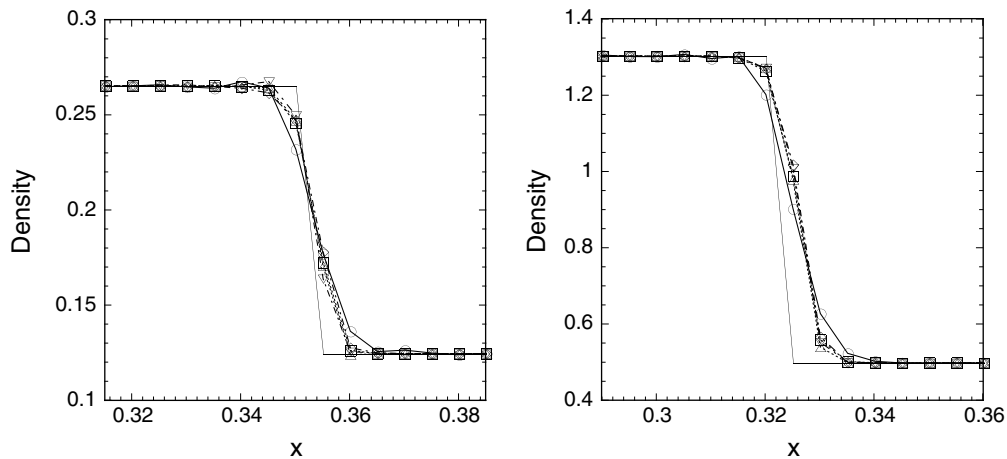
(a) Shock discontinuity: Sod problem (left), Lax problem (right)

(b) Contact discontinuity: Sod problem (left), Lax problem (right)

Fig. 19. Comparison between the numerical methods for 1D Sod and Lax shock tube problems with $\Delta x = 0.005$. Close-up views of density in the shock and contact discontinuity regions are presented at $t = 0.2$ for Sod problem and $t = 0.13$ for Lax problem. Thin solid line, exact; thick solid line with circle, LADG-C6; dotted line with square, WENO7; dotted line with triangle up, WENO9; dashed-dot line with diamond, WCNS7; dashed-dot line with triangle down, WCNS9.

Table 1
Comparison between the numerical methods for the normalized numerical discontinuity thickness and maximum wiggles amplitude at post- and pre-shock and contact discontinuity regions on 1D Sod and Lax shock tube problems

Method	Thickness		Maximum wiggles amplitude (%)			
	Shock	Contact	Pre-shock	Post-shock	Pre-contact	Post-contact
(a) Sod shock tube problem						
LADG-C6	2.94	3.68	1.30	1.57	4.75	2.07
WENO7	2.35	3.55	1.62×10^{-2}	4.98×10^{-2}	0.27	0.46
WENO9	2.29	3.09	0.44	0.21	4.13	1.27
WCNS7	2.35	3.55	5.18×10^{-3}	0.13	0.28	0.19
WCNS9	2.26	3.30	1.54×10^{-2}	1.62	0.54	0.28
(b) Lax shock tube problem						
LADG-C6	2.80	3.29	1.42×10^{-2}	0.82	0.69	1.30
WENO7	2.28	3.53	1.79×10^{-3}	6.09×10^{-2}	0.83	3.09×10^{-3}
WENO9	2.20	3.41	8.20×10^{-4}	0.20	4.01	2.48×10^{-3}
WCNS7	2.29	3.61	8.22×10^{-3}	3.06×10^{-2}	0.00	5.12×10^{-3}
WCNS9	2.24	3.30	1.44×10^{-2}	0.12	0.13	6.89×10^{-3}
MPWENO9	2.21	3.42	3.45×10^{-14}	0.11	0.68	1.25×10^{-2}

than the WENO and WCNS, the level of wiggles is relatively small except at the pre-contact discontinuity region in Sod problem. The more than 4% under-shoot at the pre-contact region in Sod problem is observed for the LADG-C6 and WENO9. The under-shoot is caused by the initial start-up error generated by the initial discontinuity [22]. The WCNS9 at the post-shock region in Sod problem introduces similar level of wiggles amplitude compared with the LADG-C6. The WENO9 introduces a large over-shoot (4%) at the pre-contact region in Lax problem. The over-shoot can be reduced to the similar level of the LADG-C6 using monotonicity preserving limiters as shown in MPWENO9.

Fig. 20 shows the comparison between the numerical methods for 1D shock–entropy wave interaction problem at the time of t = 1.8. Close-up view of density in the post-shock region is presented. The LADG method shows superior performance in resolving the entropy waves behind the shock compared to seventh- and ninth-order WENO/WCNS. This is due to the high-resolution characteristics of the compact differencing scheme, which achieve better representation of the entropy wave while the shock is captured by locally adding artificial diffusivity that does not affect the smooth regions. WENO and WCNS show the similar performance in resolving the entropy wave.

The compact differencing scheme with the artificial diffusivity scheme does not show significant detrimental effect on capturing the moving discontinuities and shows superior performance in the shock–entropy wave interaction using less stencils and computational cost compared with the high-order WENO and WCNS. The comparisons between the compact scheme with LADG method and high-order WENO/WCNS illustrate the advantage of the LADG method for the simulation of flows involving shocks, turbulence and their interactions if the small level of wiggles near discontinuity is accepted as a practical compromise. The artificial diffusivity scheme smears the discontinuities over a fixed number of grid points to
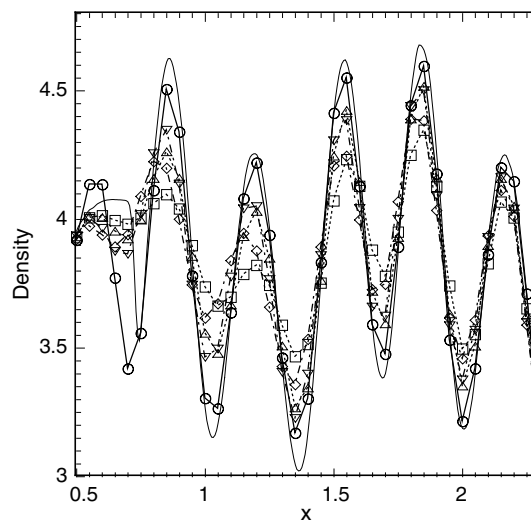
Fig. 20. Comparison between the numerical methods for 1D Shu–Osher problem with Δx = 0.05. Close-up views of density in the post-shock region is presented at t = 1.8. Thin solid line, reference solution obtained on 1601 grid points with WCNS9 [19]; thick solid line with circle, LADG-C6; dotted line with square, WENO7; dotted line with triangle up, WENO9; dashed-dot line with diamond, WCNS7; dashed-dot line with triangle down, WCNS9.

a numerically resolvable scale. Basically, slightly more smeared shock and contact discontinuities are obtained by the artificial diffusivity scheme compared with the high-order WENO/WCNS, but the actual difference in the number of grid points used to capture the discontinuities is less than one grid point.

3.5. Two-dimensional double Mach reflection

The first 2D shock test case on a uniformly spaced Cartesian mesh is the double Mach reflection problem initially used to compare several numerical schemes by Woodward and Collela [23]. Since the shock waves and contact discontinuities are not aligned with the grid, this problem can be used to assess the impact of the cross-derivative terms on the results using a
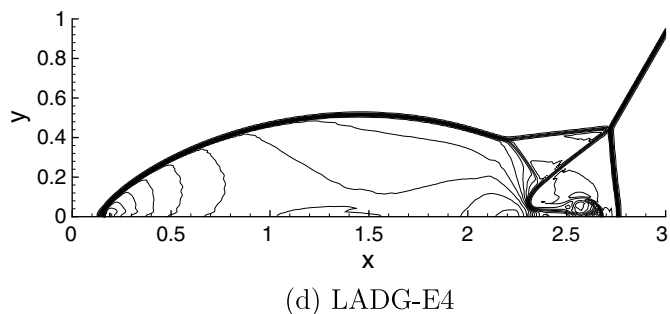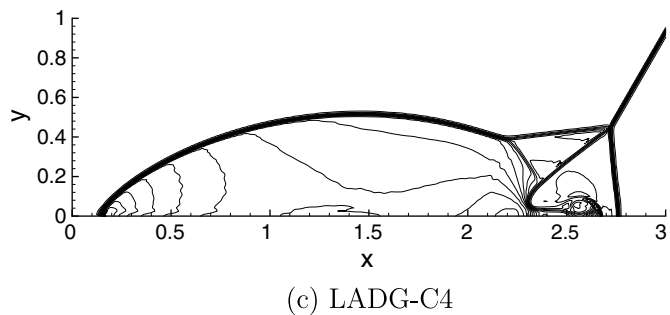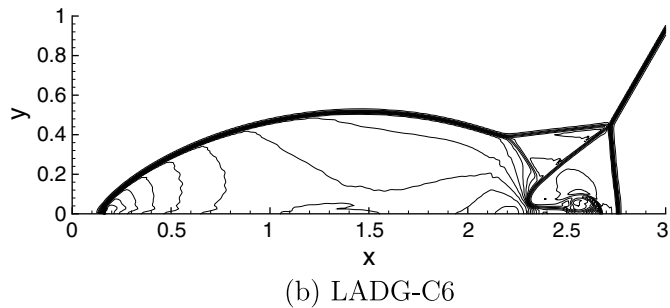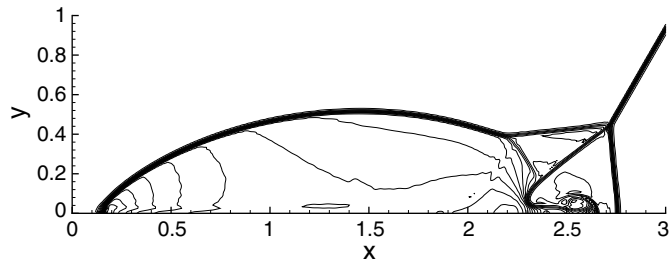

Fig. 21. Numerical simulations of the double Mach reflection of a Mach 10 shock with $\Delta x = \Delta y = 1/120$. Density, 30 equally spaced contours from 1.731 to 20.92 at $t = 0.2$.

Cartesian mesh. The original artificial diffusivity formulations [13] in Eqs. (11)–(14) include the cross-derivative term of $\frac{\partial^4 f}{\partial^2 x \partial^2 y}$, whereas the generalized multi-dimensional formulations in Eqs. (17)–(20) do not have the cross term.

Initially, a Mach 10 shock wave is at a 60° angle with a reflecting wall and intersects the bottom boundary at $x = 1/6$ and $y = 0$. The air ahead of the shock is stationary with a density of 1.4 and a pressure of 1. The conditions at the top boundary are set to describe the exact motion of the Mach 10 shock. Therefore, the Mach 10 shock keeps the 60° angle and moves to the right in the domain. The interaction with the wall creates a double Mach reflection of the shock at the wall. The conditions from $x = 0$ to $1/6$ at the bottom boundary are fixed as the conditions of the initial post-shock flow and reflecting wall conditions are used from $x = 1/6$. The values at the left boundary are fixed to the initial post-shock values, and zero-gradient conditions are employed at the right boundary. Simulations are carried out on a uniformly spaced Cartesian grid with three
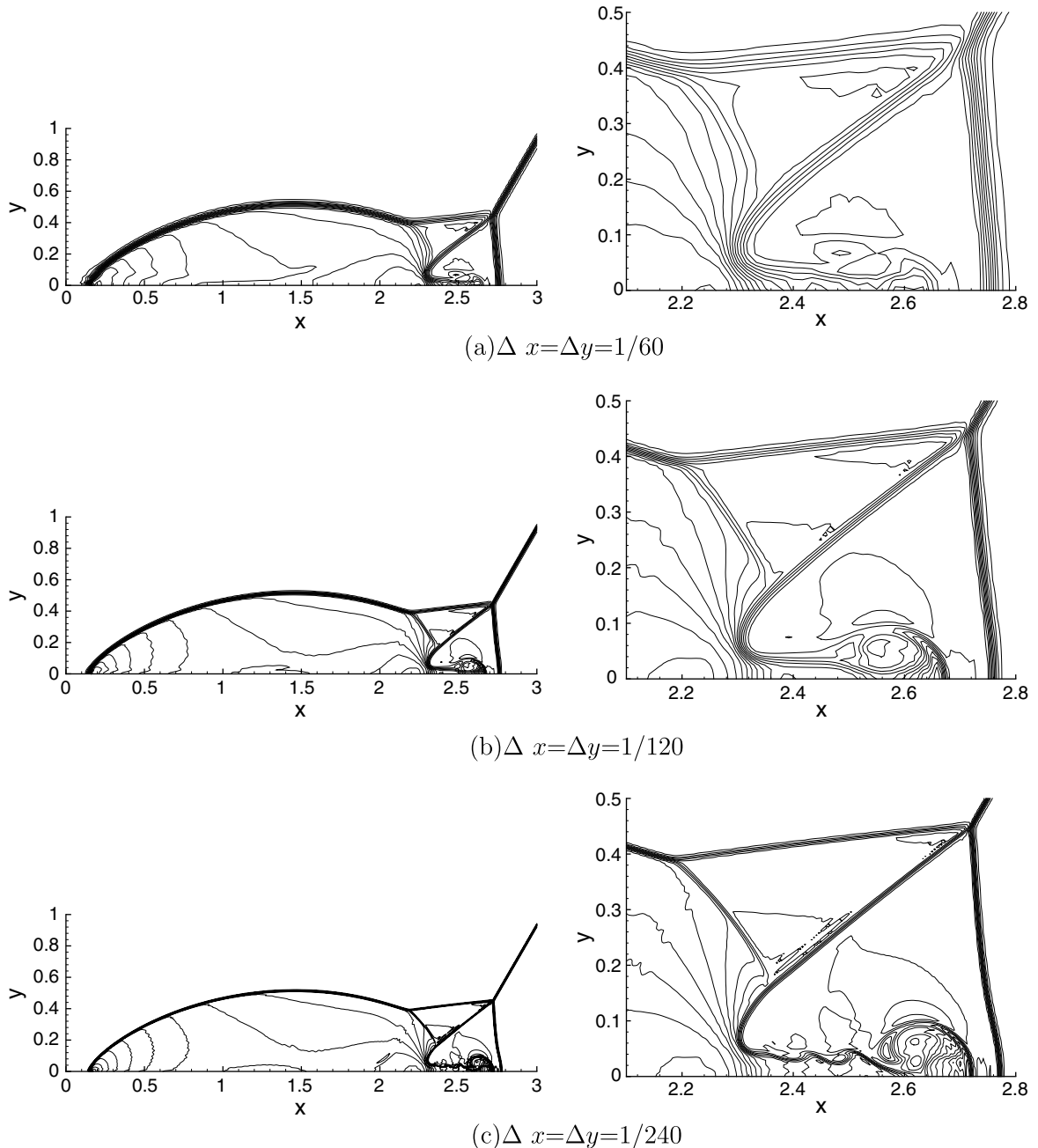

(a)$\Delta\ x=\Delta y=1/60$

(b)$\Delta\ x=\Delta y=1/120$

(c)$\Delta\ x=\Delta y=1/240$

Fig. 22. Numerical simulations of the double Mach reflection of a Mach 10 shock with $\Delta x = \Delta y = 1/60$, $1/120$ and $1/240$ obtained by LADG-C6. Density, 30 equally spaced contours from 1.731 to 20.92 at $t = 0.2$.

different levels of grid spacing 241 × 121, 481 × 241 and 961 × 481 grid points in the x- and y-directions where the computational domain extends from $x = 0$ to 4 and $y = 0$ to 2 with $\Delta x = \Delta y = 1/60$, 1/120 and 1/240.

Density contours with 30 equally spaced contours from 1.731 to 20.92 in the region $x \in [0,3]$ and $y \in [0,1]$ at the time $t = 0.2$ are plotted in Fig. 21. The results are obtained by the LAD-C6 and LADG methods using the grid spacing of $\Delta x = \Delta y = 1/120$. All the results are nearly identical. The results of the LADG scheme that ignore the cross-derivative term do not show any significant detrimental effect on the discontinuity capturing. Two-dimensional shock interactions and contact discontinuities including the near-wall jet are well captured at the proper locations in the simulations, which are sensitive to the numerics and difficult to capture. Fig. 22 shows the density contours of double Mach reflection with three different levels of grid spacing $\Delta x = \Delta y = 1/60$, 1/120 and 1/240 using the LADG-C6 method. Consistent with the mesh refinement study of the stationary normal shock wave and contact discontinuity in Sections 3.1.2 and 3.1.3, the discontinuities are captured approximately by the fixed number of grid points. Thus, the discontinuities are sharpened by refining the mesh. Roll-up of the near-wall jet is better resolved with increasing the mesh resolution. High-resolution characteristics of the present sixth-order compact differencing scheme can achieve better representation of the wall jet compared with the same grid resolution using a fifth-order WENO scheme [24] and have qualitatively similar jet compared with twice the grid resolution using a fifth-order WENO [25] while shock and contact discontinuities are captured by adding the localized artificial diffusivity to suppress high-wavenumber wiggles. Note that the fifth-order WENO uses seven points in the stencil to evaluate a spatial derivative and requires higher computational cost than the compact scheme with the artificial diffusivity. Also, qualitatively similar result is obtained by a ninth-order MPWENO [20] that requires 11 points in the stencil. The result obtained by a ninth-order WENO (without monotonicity preserving limiters) [25] shows similar near-wall jet structure but vortex structures appearing from the contact discontinuity that emerges from the triple-point are better captured than that of LADG method. This is probably due to the fact that the artificial diffusivity scheme smears the discontinuity over a numerically resolvable scale, whereas the WENO captures the discontinuity that is slightly thinner than that obtained by the LADG method as discussed in Section 3.4.

On this 2D simulation, the LADG-E4 reduces the cost for calculating the localized artificial diffusivity by a factor of 2.79 compared with the LAD-C6. This leads to a reduction of approximately 27% in the total computational cost.

3.6. Two-dimensional oblique shock reflection

The second 2D shock test case is an oblique shock reflection on an inviscid wall. The shock angle is 33° with the Mach 3 freestream. Isotropic and anisotropic Cartesian meshes are used to test the generalized model on a multi-dimensional formulation. This problem can be used to assess the capability of the generalized method on isotropic and anisotropic Cartesian meshes.
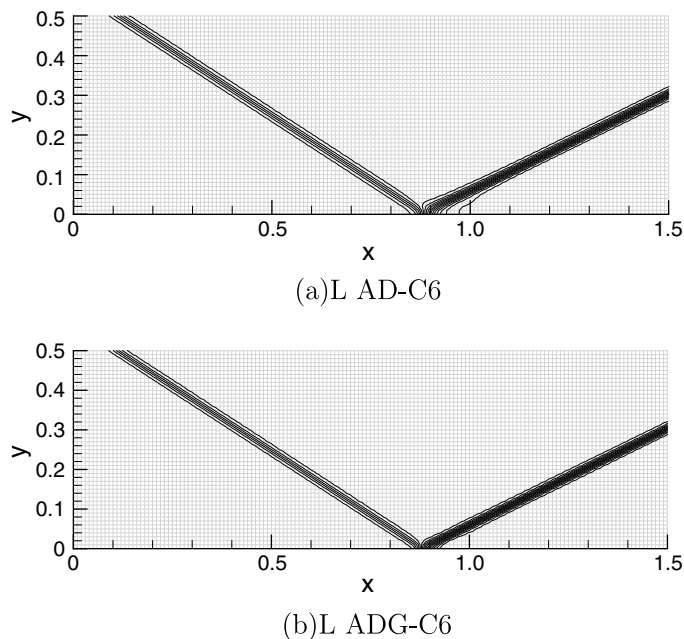

(a)L AD-C6

(b)L ADG-C6

Fig. 23. Numerical simulations of the Mach 3 oblique shock reflection on an isotropic mesh ($\Delta x = \Delta y = 0.01$). Pressure, 20 equally spaced contours from 1.2 to 7.5.
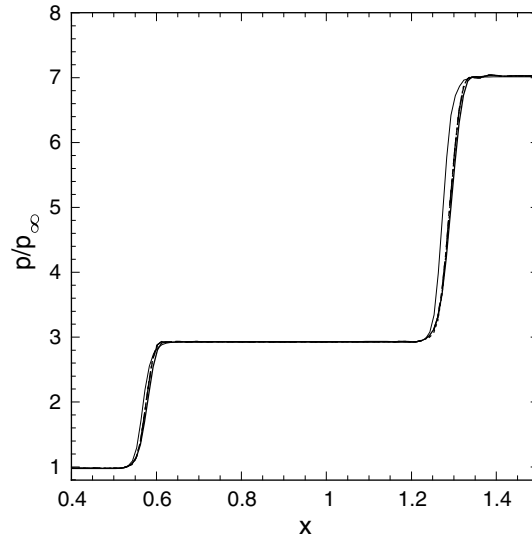
Fig. 24. Pressure profiles along y = 0.18 of the 2D Mach 3 oblique shock reflection with $\Delta x = \Delta y = 0.01$. Thin solid line, Roe scheme; thick solid line, LAD-C6; dashed line, LADG-C6; dashed-dot line, LADG-C4; dotted line, LADG-E4.

The computational domain extends from x = −1.5 to 2.0 and y = 0 to 1.5 where the isotropic mesh consists of 351×151 grid points in the x- and y-directions ($\Delta x = \Delta y = 0.01$) and the mesh aspect ratio of the anisotropic mesh is 5 ($\Delta x = 0.05$, $\Delta y = 0.01$). The shock jump conditions across one grid point and slip-wall conditions are imposed on the upper and lower boundaries, respectively. Inflow conditions are fixed to the freestream and outflow conditions are extrapolated.

3.6.1. On an isotropic mesh

Pressure contours in the region $x \in [0, 1.5]$ and $y \in [0, 0.5]$ obtained by the LAD-C6 and LADG-C6 on an isotropic mesh are plotted in Fig. 23. The results of the LADG-C4 and LADG-E4 are nearly identical to the LADG-C6 (not shown here). Pressure profiles along y = 0.18 line for the LAD-C6 and LADG schemes are shown in Fig. 24. All the simulations allow for converged solutions without significant wiggles even though the shock wave is not aligned with the mesh. Almost identical results are obtained by the LAD and LADG methods. Although the shock wave is slightly smeared compared with Roe's third-order upwind scheme, the proper post-shock conditions are well-recovered.

3.6.2. On an anisotropic mesh

Pressure contours and pressure profiles along y = 0.18 line obtained by the LAD-C6 and LADG schemes on the anisotropic mesh ($\Delta x = 5\Delta y$) are plotted in Figs. 25 and 26. The pressure contours of LADG-C4 and LADG-E4 are not presented here because all the LADG methods show almost identical results. Although all the simulations achieve converged solutions, the shock reflection is not properly simulated by the original formulation (LAD-C6) and the reflected shock wave is considerably smeared because of the undesirable mesh dependency of the artificial diffusivity. On the other hand, the LADG methods work well to capture the shock wave at the location similar to that of the Roe scheme. Consistent with the isotropic test case 3.6.1, the shock is slightly smeared compared with the Roe scheme but the proper post-shock conditions are well recovered.

3.7. Two-dimensional supersonic blunt body flow

The third 2D test case is a blunt body in a Mach 3 inviscid flow [24]. The simulations are carried out on a curvilinear anisotropic mesh where the grid is aligned with the body and the grid spacing perpendicular to the front bow shock is smaller than that in the other direction. This test case allows us to investigate the capability of the multi-dimensional curvilinear and anisotropic mesh formulations of the localized artificial diffusivity scheme. The effect of the cross-derivative terms can also be assessed for a generalized coordinate system.

An impulsive start of freestream Mach number 3 is imposed on the simulations. Therefore, the Mach 3 front bow shock gradually develops from the blunt body toward the left. Reflecting wall conditions are imposed on the blunt body, and the inflow boundary conditions are fixed to freestream conditions. Fourth-order extrapolation is employed at the outflow boundaries. A curvilinear and anisotropic mesh of 81×61 is analytically generated by using [24]:

$$x = -(R_x - (R_x - 1)\eta)\cos(\theta(2\xi - 1)), \tag{39}$$
$$y = (R_y - (R_y - 1)\eta)\sin(\theta(2\xi - 1)), \tag{40}$$

where the parameters are set to $R_x = 3$, $R_y = 6$, and $\theta = 5\pi/12$.
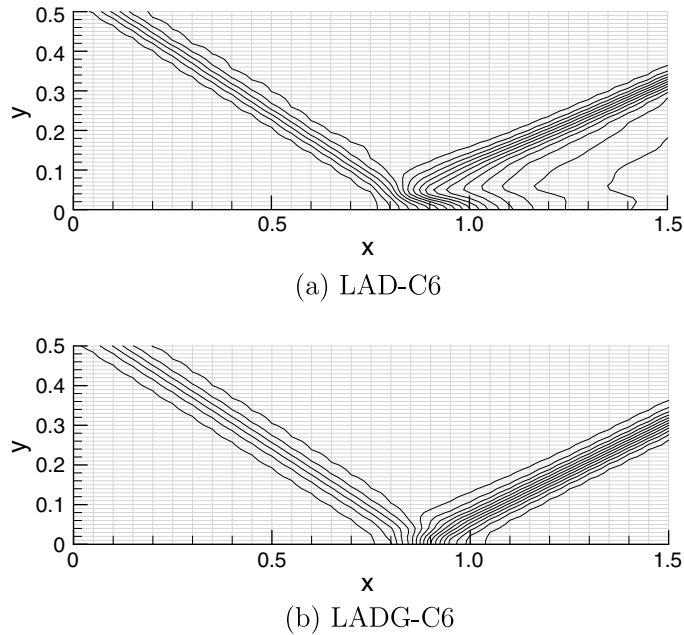
(a) LAD-C6

(b) LADG-C6

Fig. 25. Numerical simulations of the Mach 3 oblique shock reflection on an anisotropic mesh ($\Delta x = 0.05$, $\Delta y = 0.01$). Pressure, 20 equally spaced contours from 1.2 to 7.5.
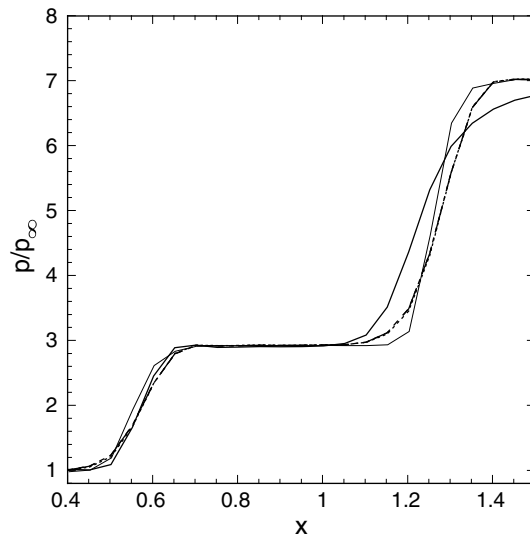

Fig. 26. Pressure profiles along $y = 0.18$ of the 2D Mach 3 oblique shock reflection with $\Delta x = 0.05$ and $\Delta y = 0.01$. Thin solid line, Roe scheme; thick solid line, LAD-C6; dashed line, LADG-C6; dashed-dot line, LADG-C4; dotted line, LADG-E4.

Fig. 27 displays pressure contours (a)–(d), artificial viscosity distributions (e) and (f), and the computational grid (g). Pressure profiles along the centerline $y = 0$ are plotted in Fig. 28. Only the LAD-C6 could not achieve a converged solution. Therefore the result of LAD-C6 shows the snapshot after a long period at the computational time $t = 20$. The LAD-C6 shows relatively high and non-smooth distribution of artificial viscosity near the bow shock region compared with the LADG-C6. This is due to the undesirable effects from the geometrically averaged grid spacing. For LAD-C6, the artificial viscosity smears the bow shock over 10 grid points and induces non-physical oscillation in the front bow shock. On the other hand, the multi-dimensional curvilinear mesh formulations proposed here works well. The LADG-C6, LADG-C4 and LADG-E4 show the converged solutions without spurious oscillations and provide almost identical results. The LADG-C6, LADG-C4 and LADG-E4
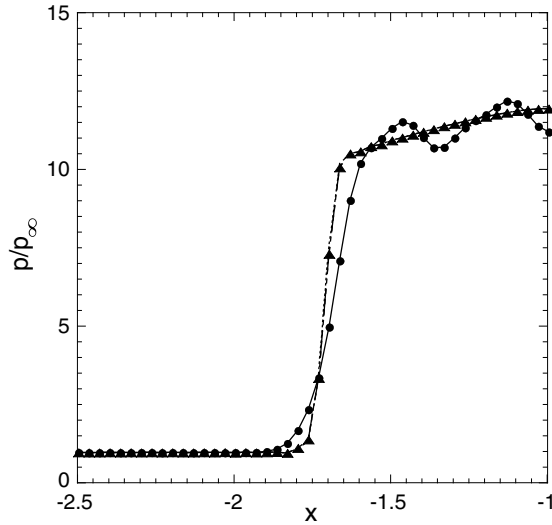
Fig. 28. Pressure profiles along centerline $y = 0$ of the 2D Mach 3 blunt body flow. Solid line with filled circle, LAD-C6; dashed line with filled triangle, LADG-C6; dashed-dot line, LADG-C4; dotted line, LADG-E4.

3.8. Two-dimensional material advection

The last test case is an inviscid 2D material advection of a circular blob in a uniform flow on isotropic Cartesian and wavy meshes. This test case can be used to investigate the capability of generalized form of D_k^* to capture the 2D moving material interface.

The initial material field is: $Y = 1$ for $r^2 < 1$ and $Y = 0$ for $r^2 \geqslant 1$, where $r^2 = ((x - x_c)^2 + (y - y_c)^2)/R_c^2$. Sharp 2D material interface across one grid point are initially imposed. Although the sharp interface remains as its initial state for immiscible fluids, the artificial diffusivity D_k^* smears the sharp interface over a numerically resolvable scale to capture the discontinuity.
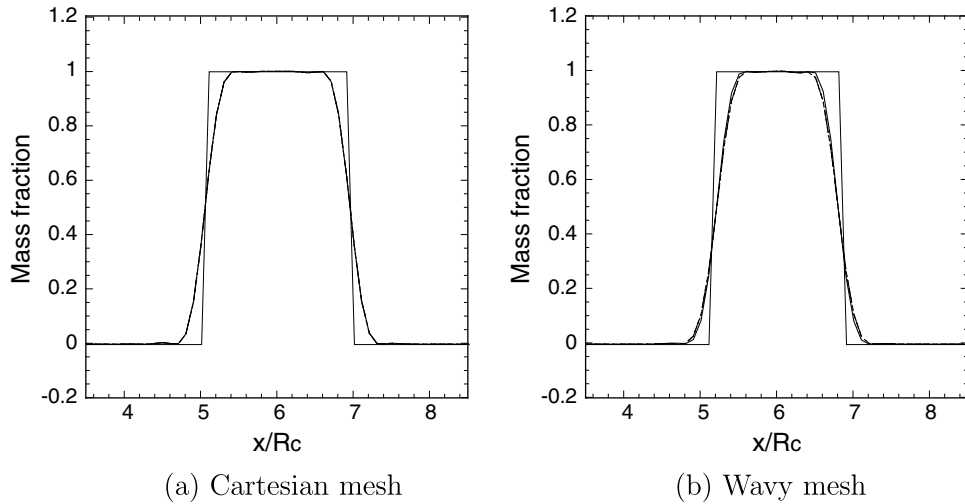

(a) Exact

(a) Cartesian mesh　　　　　　　　(b) Wavy mesh
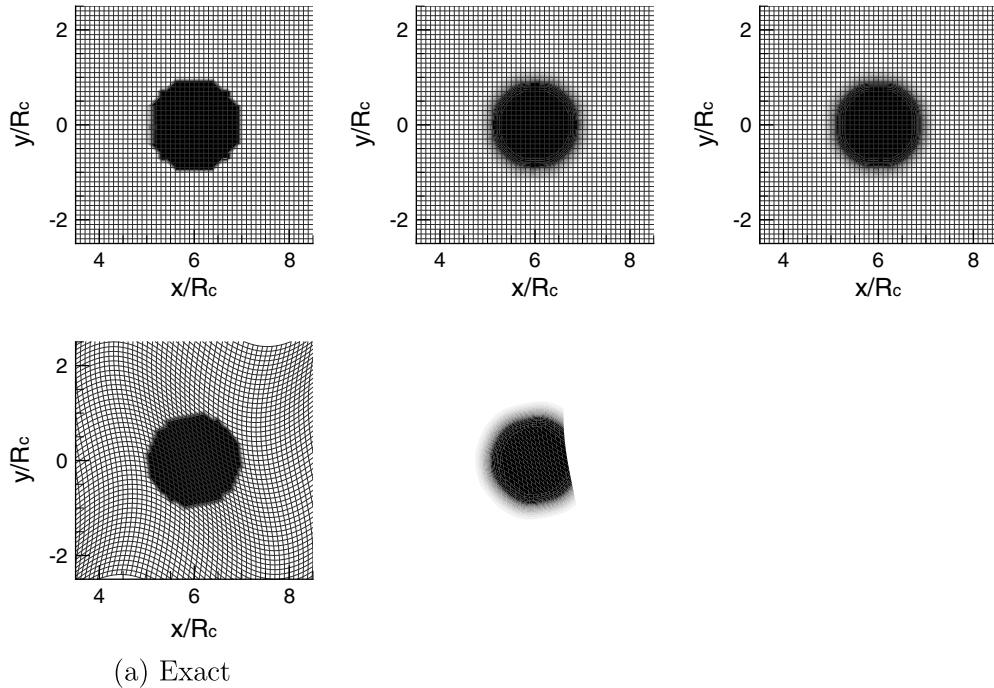
Fig. 30. Mass fraction profiles along a *j*-constant line that passes through center of the circular blob on isotropic Cartesian and wavy meshes with $\Delta x/R_c = \Delta y/R_c = 0.1$ at the time of $tU_\infty/R_c = 6$. Thin solid line, exact; thick solid line, LAD-C6; dashed line, LADG-C6; dashed-dot line, LADG-C4; dotted line, LADG-E4.

The uniform freestream Mach number and center of the circular blob are: $M_\infty = 0.1$ and $x_c = y_c = 0$. Four different levels of mesh size $\Delta x/R_c = \Delta y/R_c = 0.1, 0.15, 0.2$ and 0.3 are employed for both the isotropic Cartesian and wavy meshes. The computational domain for the isotropic Cartesian mesh extends $-3 \leqslant x/R_c \leqslant 9$ and $-3 \leqslant y/R_c \leqslant 3$. The wavy meshes are generated in the same manner as Section 3.1.1 using Eqs. (33) and (34) with $x_{\min} = y_{\min} = -3$, $L_x = 12$, $L_y = 6$, $n_x = 2$, $n_y = 4$, $A_x = 0.2R_c/\Delta x$, and $A_y = 0.8R_c/\Delta y$. Periodic boundary conditions are applied on both the boundaries in the *i*- and *j*-direction.

Mass fraction distributions in the region $x/R_c \in [3.5, 8.5]$ and $y/R_c \in [-2.5, 2.5]$ obtained by the LAD-C6 and LADG-C6 on the isotropic Cartesian and wavy meshes with $\Delta x/R_c = \Delta y/R_c = 0.1$ are compared with the exact solution in Fig. 29. The results of the LADG-C4 and LADG-E4 are nearly identical to the LADG-C6 and not shown here. The mass fraction profiles along a *j*-constant line that passes through the center of the circular blob for the LAD-C6 and LADG schemes with $\Delta x/R_c = \Delta y/R_c = 0.1$ are shown in Fig. 30. Table 2 summarizes the error in the total mass conservation defined by

$$\text{Error} = \frac{|\iint_S (\rho Y - \rho_{ex} Y_{ex}) dS|}{\iint_S \rho_{ex} Y_{ex} dS}, \tag{41}$$

where the ex subscripts denote the value of exact solution. Note that D_k^* model proposed in this paper is different from the original model of Cook [13]. D_k^* for the LAD-C6 is evaluated by the following formula:

$$D_k^* = C_D c_s \overline{|\nabla^2(\nabla^2 Y_k)| \Delta^{r+1}} + C_Y c_s \overline{[Y_k - 1] H(Y_k - 1) - Y_k[1 - H(Y_k)]} \Delta, \tag{42}$$

and D_k^* for the LADG scheme is evaluated by using Eq. (20). The results are obtained at the time of $tU_\infty/R_c = 6$ where the circular blob convects the distance of $6R_c$. The initial sharp material interface is captured well by smearing the discontinuity to a numerically resolvable scale using the localized artificial diffusivity D_k^*. The total mass of ρY is conserved within the admissible error (order of 10^{-4} or less) and the mass fraction keeps the bounds of $0 \leqslant Y \leqslant 1$ well for all the cases. The error in the

Table 2
Error in the total mass conservation on 2D material advection of a circular blob

Method	Error in total mass conservation			
	$\Delta x/R_c = \Delta y/R_c = 0.3$	$\Delta x/R_c = \Delta y/R_c = 0.2$	$\Delta x/R_c = \Delta y/R_c = 0.15$	$\Delta x/R_c = \Delta y/R_c = 0.1$
(a) Cartesian mesh				
LAD-C6	1.87×10^{-4}	1.60×10^{-4}	7.29×10^{-5}	1.28×10^{-6}
LADG-C6	1.99×10^{-4}	1.71×10^{-4}	6.62×10^{-5}	2.44×10^{-7}
LADG-C4	2.00×10^{-4}	1.72×10^{-4}	6.63×10^{-5}	5.03×10^{-8}
LADG-E4	2.06×10^{-4}	1.81×10^{-4}	7.07×10^{-5}	2.09×10^{-6}
(b) Wavy mesh				
LAD-C6	7.02×10^{-4}	1.75×10^{-4}	6.01×10^{-5}	8.24×10^{-6}
LADG-C6	8.20×10^{-4}	2.06×10^{-4}	7.28×10^{-5}	5.95×10^{-6}
LADG-C4	8.16×10^{-4}	2.06×10^{-4}	7.30×10^{-5}	5.28×10^{-6}
LADG-E4	7.81×10^{-4}	1.98×10^{-4}	7.36×10^{-5}	2.13×10^{-5}

mass conservation is quite small even if the relatively coarse meshes with $\Delta x/R_c = \Delta y/R_c = 0.3$ are used where 6–7 grid points are located across the blob. Nearly, identical results are obtained by the LAD and LADG methods both on the Cartesian and wavy meshes. The results of the LADG schemes that ignore all the cross-derivative terms do not show any significant detrimental effect.

4. Conclusions

A simple and efficient localized artificial diffusivity scheme has been developed for the purpose of capturing discontinuities in a multi-dimensional generalized coordinate framework using a high-order compact differencing scheme. The artificial diffusivity is dynamically localized in space to capture different types of discontinuities. The method is essentially based on the original 1D formulation proposed by Cook [13]. Computational efficiency benefit comes from approximating the double Laplacians with the direct implementation of fourth derivatives.

Analysis for the performance of the method on smooth and non-smooth flows has been conducted on isotropic Cartesian and wavy meshes. The LADG method on both the isotropic and wavy meshes successfully captures the discontinuities with minimal effects by smearing the discontinuities over a numerically resolvable scale and does not show major impact on the smooth flows. The amplitude of wiggles near discontinuity and the number of grid points to capture the discontinuity do not depend on the mesh size.

The comparisons between the compact scheme with LADG method and high-order WENO/WCNS on the 1D shock-related problems illustrate the advantage of the LADG method for the simulation of flows involving shocks, turbulence and their interactions.

The method has been successfully applied to several 1D and 2D, steady and unsteady complex discontinuity-related problems on isotropic and anisotropic Cartesian meshes and an anisotropic curvilinear mesh. The generalized formulation maintains the properties of the original 1D formulation. All the cases examined in this paper indicate that the simplification of the method does not show any major detrimental effect on both the smooth and non-smooth flows (discontinuity capturing) while reducing computational cost.

The LADG method reduces the cost for calculating the localized artificial diffusivity compared with the original double Laplacians formulations and works well on curvilinear and anisotropic meshes. Almost identical results are obtained by using the different schemes that evaluate the fourth derivatives in the generalized formulations of localized artificial diffusivity scheme. Therefore the LADG-E4 method can be an attractive choice for further reducing computational costs when the method is applied to practical applications on a multi-dimensional generalized coordinate system. The authors used this artificial diffusivity method to simulate the mixing of a 3D under-expanded sonic jet into a supersonic crossflow [26], showing the applicability of this approach for the LES of compressible flow involving shocks, contact surfaces, material discontinuities, turbulence and their interactions. Results for further calculations with the artificial diffusivity scheme presented in this paper will be reported in future.

References

[1] S.K. Lele, Compact finite difference schemes with spectral-like resolution, Journal of Computational Physics 103 (1) (1992) 16–42.
[2] M.R. Visbal, D.V. Gaitonde, High-order-accurate methods for complex unsteady subsonic flows, AIAA Journal 37 (10) (1999) 1231–1239.
[3] D.P. Rizzetta, M.R. Visbal, Large-eddy simulation of supersonic cavity flowfields including flow control, AIAA Journal 41 (8) (2003) 1452–1462.
[4] B. Rembold, L. Kleiser, Noise prediction of a rectangular jet using large-eddy simulation, AIAA Journal 42 (9) (2004) 1823–1831.
[5] S. Lee, S.K. Lele, P. Moin, Interaction of isotropic turbulence with shock waves: effect of shock strength, Journal of Fluid Mechanics 340 (1997) 225–247.
[6] C.W. Shu, S.J. Osher, Efficient implementation of essentially nonoscillatory shock capturing schemes II, Journal of Computational Physics 83 (1) (1989) 32–78.
[7] D.P. Rizzetta, M.R. Visbal, D.V. Gaitonde, Large-eddy simulation of supersonic compression-ramp flows by high-order method, AIAA Journal 39 (12) (2001) 2283–2291.
[8] P.L. Roe, Approximate Riemann solvers, parameter vectors, and difference scheme, Journal of Computational Physics 43 (2) (1981) 357–372.
[9] M.R. Visbal, D.V. Gaitonde, Shock capturing using compact-differencing-based method, AIAA Paper 2005-1265, AIAA, 2005.
[10] A.W. Cook, W.H. Cabot, A high-wavenumber viscosity for high-resolution numerical method, Journal of Computational Physics 195 (2) (2004) 594–601.
[11] A.W. Cook, W.H. Cabot, Hyperviscosity for shock–turbulence interactions, Journal of Computational Physics 203 (2) (2005) 379–385.
[12] B. Fiorina, S.K. Lele, An artificial nonlinear diffusivity method for supersonic reacting flows with shocks, Journal of Computational Physics 222 (1) (2007) 246–264.
[13] A.W. Cook, Artificial fluid properties for large-eddy simulation of compressible turbulent mixing, Physics of Fluids 19 (5) (2007) 055103.
[14] D.V. Gaitonde, M.R. Visbal, Padé-type higher-order boundary filters for the Navier–Stokes equations, AIAA Journal 38 (11) (2000) 2103–2112.
[15] D.V. Gaitonde, J.S. Shang, J.L. Young, Practical aspects of high-order accurate finite-volume schemes for electromagnetics, AIAA Paper 97-0363, AIAA, 1997.

[16] T.J. Poinsot, S.K. Lele, Boundary conditions for direct simulations of compressible viscous flows, Journal of Computational Physics 101 (1) (1992) 104–129.

[17] G.A. Sod, A survey of several finite difference methods for systems on non-linear hyperbolic conservation laws, Journal of Computational Physics 27 (1) (1978) 1–31.

[18] P.D. Lax, Weak solutions of nonlinear hyperbolic equations and their numerical computation, Communications on Pure and Applied Mathematics 7 (1) (1954) 159–193.

[19] T. Nonomura, N. Iizuka, K. Fujii, Increasing order of accuracy of weighted compact non-linear scheme, AIAA Paper 2007-893, AIAA, 2007.

[20] D.S. Balsara, C.W. Shu, Monotonicity preserving weighted essentially non-oscillatory schemes with increasingly high order of accuracy, Journal of Computational Physics 160 (2) (2000) 405–452.

[21] X.G. Deng, H. Zhang, Developing high-order weighted compact nonlinear schemes, Journal of Computational Physics 165 (2000) 22–44.

[22] M. Arora, P.L. Roe, On postshock oscillations due to shock capturing schemes in unsteady flows, Journal of Computational Physics 130 (1) (1997) 25–40.

[23] P. Woodward, P. Collela, The numerical simulation of two-dimensional fluid flow with strong shock, Journal of Computational Physics 54 (1) (1984) 115–173.

[24] G.S. Jiang, C.W. Shu, Efficient implementation of weighted ENO scheme, Journal of Computational Physics 126 (1) (1996) 202–228.

[25] J. Shi, Y.T. Zhang, C.T. Shu, Resolution of high order WENO schemes for complicated flow structures, Journal of Computational Physics 186 (2) (2003) 690–696.

[26] S. Kawai, S.K. Lele, Mechanisms of jet mixing in a supersonic crossflow: a study using large-eddy simulation, AIAA Paper 2008-4575, AIAA, 2008.